CONTROL OF BUDDED DOMAINS IN AMPHIPHILIC BILAYER MEMBRANES

by

William Eric Uspal

Submitted to the University

Honors College in partial fulfillment

of the requirements for the degree of

Bachelor of Philosophy

University of Pittsburgh

2007

UNIVERSITY OF PITTSBURGH

UNIVERSITY HONORS COLLEGE

This thesis was presented

by

William E. Uspal

It was defended on

April 4, 2007

and approved by

Michael J. Fasolka, Polymers Division, NIST

Adam K. Leibovich, Physics and Astronomy, University of Pittsburgh

Chandralekha Singh, Physics and Astronomy, University of Pittsburgh

Advisor: Anna C. Balazs, Chemical and Petroleum Engineering, University of Pittsburgh

CONTROL OF BUDDED DOMAINS IN AMPHIPHILIC BILAYER MEMBRANES

William Eric Uspal, B.Phil

University of Pittsburgh, 2007

Phase separated domains in multicomponent vesicles form spherical buds to reduce interfacial energy. We study the response of a multicomponent budded vesicle to an imposed shear flow with dissipative particle dynamics. We find that shear can either act to stretch the bud open or separate the bud from the vesicle, depending on bud orientation. We examine the interplay of interfacial tension, bending energy, and shear in determining the behavior of the vesicle, and provide criteria for the design of vesicles for controlled bud release.

The neck connecting the budded domain with the bulk vesicle assumes a catenoid shape to minimize bending energy. We model the mechanism for pinch-off of catenoid necks with continuum elastic theory and dissipative particle dynamics. We examine pore nucleation and growth driven by Gaussian energy, by the adhesion energy of an encapsulated particle, and by the line energy of an interface between two amphiphile species, aiming to provide principles for the design of vesicles for biomimetic phagocytosis.

TABLE OF CONTENTS

LIST OF FIGURES

ACKNOWLEDGMENTS

This thesis would not have been possible without the help of many people – too many, in fact, to name, but there are a few that deserve particular mention. Dr. Kurt Smith stands out as my closest collaborator in this research. I learned a lot from Kurt, and the reader can be assured that the good ideas are mostly his. Prof. Anna Balazs was a fantastic thesis advisor and fantastically good at finding free food in Benedum. I particularly appreciate going to the ACS and MRS conferences and her help in preparation for them. I would like to thank the committee members: Prof. Adam Leibovich, Prof. Chandralekha Singh, and especially Dr. Michael Fasolka, who traveled from NIST for the defense. Finally, I would like to thank everyone in the Soft Matter group for their support and encouragement over the past two years, as well as everyone else who attended the thesis defense. I cannot think of a better set of people with whom to start a scientific career.

1.0 INTRODUCTION

Amphiphiles contain both hydrophilic head and hydrophobic tail groups and, in sufficient concentration, spontaneously self-assemble into structures like micelles and bilayers. These structures shield the hydrophobic tail groups from the surrounding solvent, maximizing entropy. Bilayers can further reduce edge free energy by closing to form vesicles, which contain an interior pocket of solvent isolated from the external environment. Additional structure is possible in multicomponent membranes, where phase separation can be followed by the formation of mushroom-like buds that protrude from the two dimensional membrane into the surrounding three dimensional space. These buds reduce the contact length between the two different membrane domains.

Bilayer membranes and vesicles are ubiquitous in cell biology. The plasma membrane separates the cell interior and exterior, anchors the cytoskeleton, and contains a host of proteins that identify the cell and mediate interactions with the surrounding environment. Within the eukaryotic cell, biochemical reactions are often contained within membrane bound organelles, and membrane bound proteins can serve to catalyze these reactions. For instance, within the double membraned mitochondria, the molecular machinery of ATP synthase exploits a proton gradient across the inner membrane to drive synthesis of ATP. In chloroplasts, photon energy is harvested by integral proteins in stacked thylakoid membranes. Vesicles are vital to intracellular packaging and transport. In exocytosis, interior vesicles fuse with the plasma membrane,

expelling their contents without causing the loss of cytosol Likewise, in endocytosis, particles from the environment are engulfed by the plasma membrane, and the resultant bud is pinched off as an interior vesicle. While many events in the biological membrane are active, driven by metabolic energy, much remains to be understood on the basis of passive physical forces. One theoretical study, for instance, models how a membrane-bound protein, caveolin, can drive formation of an invagination or bud through the exertion of asymmetrical forces on the membrane.[1]

Furthermore, simple amphiphilic vesicles have recently begun to play an important role in industrial applications, e.g. in drug delivery by liposomes and, increasingly, block copolymersomes. Further down the road, amphiphilic bilayers could be important to soft, biomimetic nanotechnology. For instance, synthetic vesicles could be engineered to selectively remove nanoparticle contaminants from the environment in biomimetic endocytosis. Vesicles could serve as robust containers ("test tubes") for chemical reactions. More fancifully, synthetic bilayers could provide the platform for biomimetic energy harvesting and macromolecule synthesis, and deformable vesicles could circulate through the channels of microfluidic devices in the manner of human erythrocytes.

Numerous experimental, computational, and theoretical studies have been undertaken to illuminate the physical properties of bilayer membranes and vesicles. Phase separation and budding in multicomponent giant unilamellar vesicles has been resolved with florescence microscopy.[2,3] Continuum elastic theory has been applied to equilibrium shapes of multicomponent vesicles,[4] intermediates in membrane fusion[5] and membrane adhesion to colloid particles.[6] Molecular modeling has been used to study the dynamics of budding and fission,[7,8] intermediate structures in fusion, and pore nucleation in stretched membranes.[9]

However, no previous study has examined structural changes of budded multicomponent vesicles in shear flow. Understanding the dynamics of vesicles in shear flow is crucial to applications in microfluidics and drug delivery. If the conditions for shear-driven bud pinch-off were known, multicomponent vesicles could be designed to target specific flow regions for delivery of daughter vesicles ("packets") containing the interior fluid. Via coarse-grained molecular simulation, we pinpoint the conditions for pinch-off of the budded minority domain. Our results are described in Section 4.

Likewise, we know of no previous study that has closely examined the mechanism of pinch-off in the neck of membrane encapsulated particles. Understanding the physical principles of fission driven by adhesion energy is important to applications in targeted drug delivery and biomimetic phagocytosis. Via continuum elastic theory, we model the energetics of fission via pore nucleation and growth in a homogeneous membrane, in a membrane in contact with an adhesive particle, and in a membrane with an interface between two lipid species. With dissipative particle dynamics, we simulate interface and adhesion driven fission. Ultimately, we aim to connect the elastic theory with the statistics of our simulations. This work is detailed in Section 5.

The Dissipative Particle Dynamics (DPD) simulation method is described in Section 2. DPD is a coarse-grained, mesoscopic simulation scheme that is suited to the time and length scales characteristic of membrane behavior. It retains relevant details of molecular architecture while allowing a larger simulation time-step.

Preliminary to the studies of Sections 4 and 5, in Section 3 we apply the DPD method to the equilibrium conformations of single and multicomponent membranes. We show that our simulation scheme correctly reproduces the lipid density distribution and stress profile for a

bilayer membrane, and compare equilibrium vesicle shapes to those obtained in previous analytical and numerical studies. In order to connect our simulation results with continuum theory, we determine the elastic parameters K, Σ, $a_{l,0}$, κ, and κ_g as a function of DPD simulation parameters.

We summarize our results and conclude in Section 6, discussing relevance of our results for engineering applications and directions for further study.

2.0 SIMULATION METHODOLOGY

2.1 DISSIPATIVE PARTICLE DYNAMICS

Dissipative particle dynamics (DPD) is an alternative to traditional MD introduced by Hoogerbrugge and Koelman in 1992, intended to model the hydrodynamics of complex fluids.[10,11] DPD replaces the usual Lennard-Jones potential with a soft repulsive interaction that allows coarse graining in time and space. The atomistic representation of a polymer chain can be replaced by a bead-spring model, while the simulation time step can be significantly enlarged without introducing instability. This coarse graining allows access to time and length sales that are prohibitively computationally expensive in MD, while preserving relevant molecular architectural detail that continuum approaches omit. Secondly, DPD allows for recovery of hydrodynamics, as the soft repulsive interaction and all forces in the system act pairwise, are Galilean invariant, and preserve angular and linear momentum. In featuring both molecular detail and correct hydrodynamics, DPD bridges the continuum and atomistic approaches and opens opportunities for simulation of mesoscale supramolecular phenomena.

Like MD, DPD models the Newtonian time evolution of a many-body system through numerical simulation of the Second Law:

$$f_{i_i}(t) = m\frac{dv_i}{dt} = \sum_j (F_{ij}^C + F_{ij}^D + F_{ij}^R)$$

where the sum runs over all beads j within a cutoff radius r_c. The conservative force is a soft central force:

$$F_{ij}^C(t) = a_{ij}(1 - r_{ij})r_{ij}$$

The drag force is given by:

$$F_{ij}^D(t) = -\gamma\omega_D(r_{ij})(r_{ij} \cdot v_{ij})r_{ij}$$

where γ is a simulation parameter and $\omega_D(r_{ij})$ is a weight function which goes to zero at r_c. Finally, the stochastic force is

$$F_{ij}^R(t) = \alpha\omega_R(r_{ij})\xi_{ij}r_{ij}$$

where ξ_{ij} is a Gaussian distributed random variable with zero mean and unit variance. Since the thermostat forces are pairwise and act along particle separation vectors, they conserve angular and linear momentum. Here DPD can be contrasted with Brownian dynamics, which can only simulate diffusive, not hydrodynamic, phenomena. Likewise, use of relative velocity v_{ij} does not privilege any particular reference frame; the system is Galilean invariant.

Recovery of hydrodynamics imposes additional conditions on the random variable, the simulation parameters, and the weight function. In the calculation of forces for particle j, $\xi_{ij} = \xi_{ji}$. Furthermore, Espanol and Warren show that the following fluctuation-dissipation relations must hold between the dissipative and random forces:

$$\omega_D(r_{ij}) = \omega_R(r_{ij})^2$$

$$\alpha = 2k_B T\gamma$$

where one weight function can be chosen arbitrarily.[12] Groot and Warren choose:

$$\omega_D(r_{ij}) = \omega_R(r_{ij})^2 = (1 - r_{ij})^2$$

for $r_{ij} < r_c$.

Because the dissipative force, and therefore the total force, is dependent on velocity, the velocity-Verlet algorithm must be modified to be an iterative predictor-corrector scheme. Forces, velocities, and positions at time t are known; they must be calculated for time $t + \Delta t$, where Δt is the simulation timestep. The position at time $t + \Delta t$ is calculated just as it is in the ordinary velocity-Verlet algorithm:

$$r(t + \Delta t) = r(t) + v(t)\Delta t + \frac{f(t)}{2m}\Delta t^2$$

Ordinarily, the velocity $v_i(t + \Delta t)$ would be calculated from the forces $f_i(t)$ and $f_i(t + \Delta t)$:

$$v_i(t + \Delta t) = v_i(t) + \frac{f_i(t) + f_i(t + \Delta t)}{2m}\Delta t$$

However, since $f_i(t + \Delta t)$ depends on $v_i(t + \Delta t)$ as well as on $r_i(t + \Delta t)$, a prediction $v_i'(t + \Delta t)$ for velocity is calculated from the force $f_i(t)$:

$$v_i'(t + \Delta t) = v_i(t) + \lambda \Delta t f_i(t)$$

Groot and Warren choose $\lambda = ½$, as the actual velocity-Verlet algorithm would be recovered for this value if the velocity dependent force $F_{ij}^D = 0$. The updated position and predicted velocity are used to calculate the force at time $t + \Delta t$:

$$f(t + \Delta t) = f_i(r_i(t + \Delta t), v_i'(t + \Delta t))$$

Finally, this force is used to correct the velocity at time $t + \Delta t$:

$$v_i(t+\Delta t) = v_i(t) + \frac{f_i(t) + f_i(t+\Delta t)}{2m}\Delta t$$

All simulations are conducted with the open source LAMMPS package.[13]

2.2 WALL BOUNDARY CONDITIONS

The chief advantage of DPD is the use of repulsive soft potentials that allow coarse graining. However, this features presents a problem for simulation of wall-driven simple shear, for even close-packed walls of DPD particles are too soft to prevent penetration by solvent particles. Therefore, an additional boundary condition must be imposed: reflection. Specular reflection, however, does not correctly reproduce the no-slip boundary condition. One must use bounceback reflection, whereby if

$$(v_{old} \cdot n_{wall}) < 0$$

for a particle in the wall region, then its velocity is reassigned as

$$v_{new} = 2v_{wall} - v_{old}$$

A representative velocity profile is shown below:

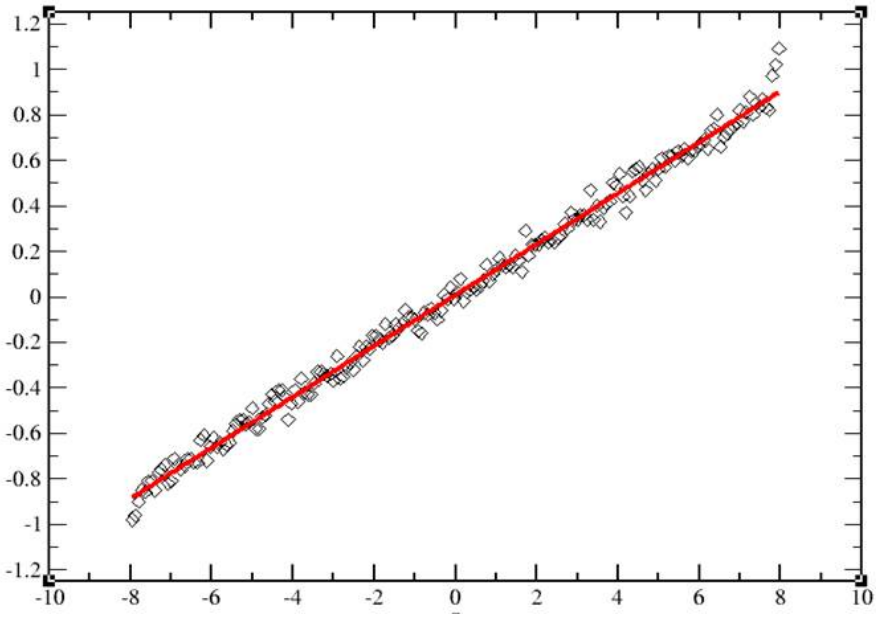

Figure 1 – Velocity profile obtained with bounceback boundary condition

2.3 DPD PARAMETERS AND AMPHIPHILE ARCHITECTURE

We take r_c as the characteristic length scale and $k_B T$ as the characteristic energy scale in our simulations. It follows that the characteristic time scale is $\tau = \sqrt{m r_c^2 / k_B T}$. We set the remaining DPD simulation parameters as noise parameter $\alpha = 3$ and timestep $\Delta t = 0.02\tau$, with a total bead number density of $\rho = 3 / r_c^3$.

We construct amphiphiles ("lipids") from beads connected by harmonic spring bonds. Each amphiphile consists of three hydrophilic head beads (H) and six hydrophobic tail beads (T), with the latter arranged in two tails:

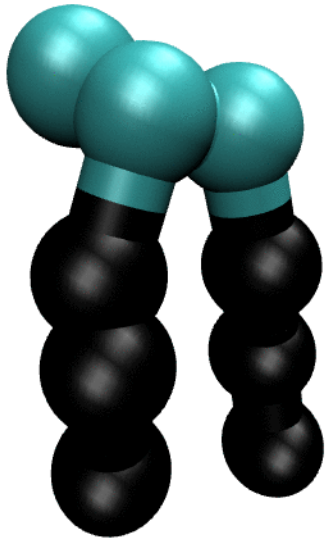

Figure 2 – Twin-tail amphiphile architecture. Cyan beads are hydrophilic head groups, and black beads are hydrophobic tail groups.

The bond potentials are:

$$E_{bond} = K_{bond}((r-b)/r_c)^2$$

where K_{bond} is the bond constant and b is the equilibrium bond length. We use $K_{bond} = 64$ and $b = 0.5$. We also insert a weaker bond ($K'_{bond} = 10$) between the first beads on the two tails to keep the tails oriented in the same direction.

An angle triple potential stiffens the tails, increasing the stability and bending rigidity of the bilayers. The form of this potential is

$$E_{angle} = K_{angle}(1+\cos\theta)$$

where θ is the angle defined by three adjacent beads. We set the coefficient to $K_{angle} = 10$ or $K_{angle} = 20$. Additionally, the amphiphiles are immersed in solvent beads (S). All beads have mass $m = 1$.

For beads of identical type, we set the DPD conservative interaction parameter to $a_{ii} = 25$. For the remaining interactions, we set $a_{HS} = 25$, $a_{HT} = 100$, and $a_{ST} = 100$. When we examine heterogeneous membranes, we further designate two head and two tail types H_1, H_2 and T_1, T_2, where the subscript indicates the lipid species. We set $a_{H_1H_2} = a_{T_1T_2} > 25$, which causes the lipids to phase separate. A homogeneous membrane is shown in Figure 3 below, and the density profile for this system is shown in Figure 4.

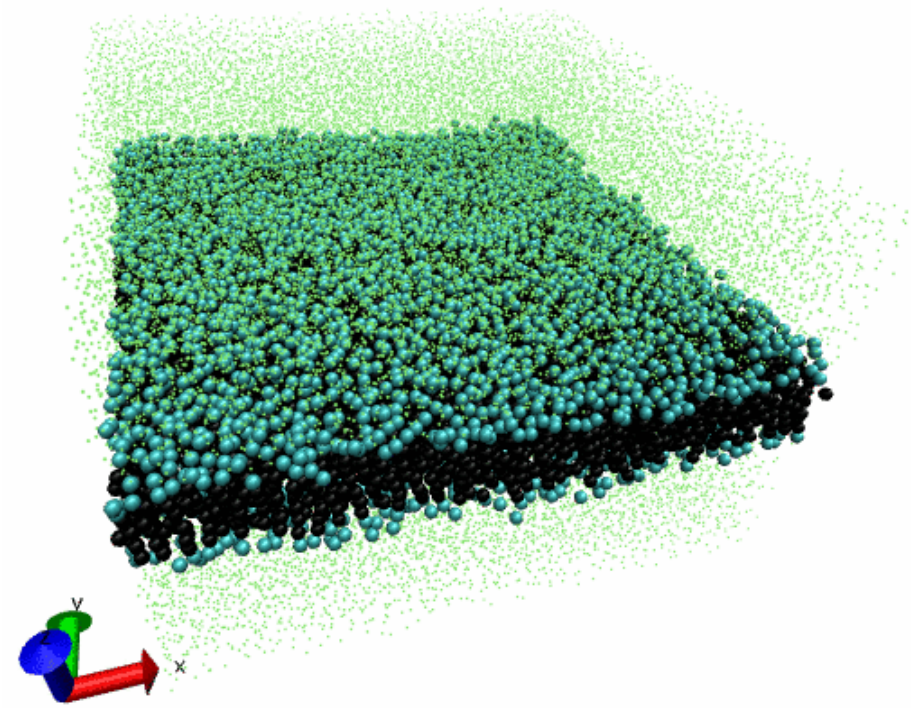

Figure 3 – A homogeneous membrane. The system is periodic in the x, y, and z directions. Cyan beans are head groups, black beads tail groups, and green points solvent particles.

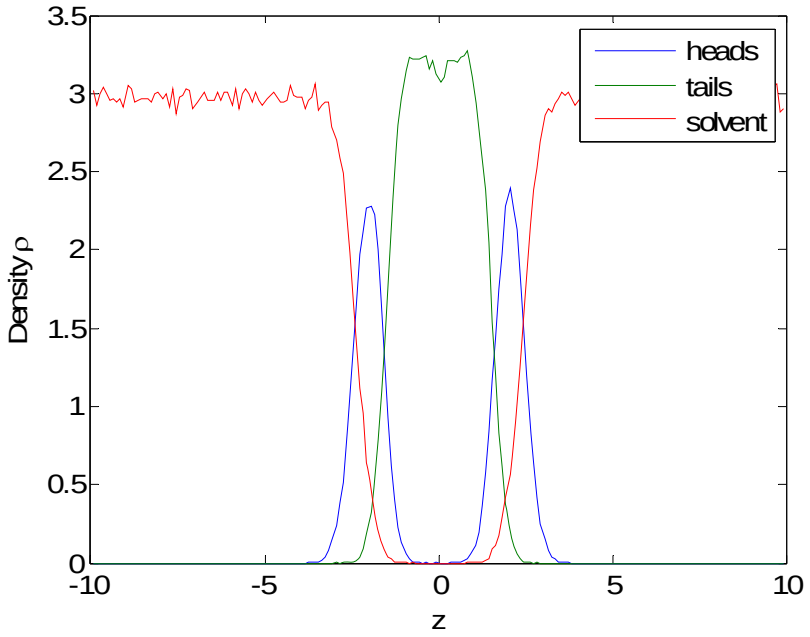

Figure 4 – Density profile in the z-direction for the membrane shown in Figure 3.

From Figure 4, we can estimate the thickness h of the membrane from the distance between the two head peaks: $h \approx 4$.

3.0 VESICLES IN EQUILIBRIUM

3.1 MEMBRANE ENERGETICS

The equilibrium conformation of a membrane is determined by minimization of the Helfrich free energy functional. For a homogeneous membrane, the free energy is the sum of mean curvature, Gaussian curvature, and stretching energies:

$$F = F_{elastic} + F_{bend}$$

The bending energy is given by

$$F_{bend} = \int dA \left[\frac{\kappa}{2} (C_1 + C_2)^2 + \kappa_G C_1 C_2 \right]$$

where C_1 and C_2 are two principal curvatures, κ the mean curvature bending modulus, and κ_G the Gaussian curvature modulus. The Gaussian term is generally neglected in calculation of membrane conformation. According to the Gauss-Bonnet theorem, the integral of Gaussian curvature over a surface is constant, provided the genus and boundaries of the surface remain the same.

For small deviations from the equilibrium area per lipid $a_{l,0}$, the stretching energy is given by

$$F_{elastic} = \frac{K}{2}\left(\frac{a_l - a_{l,0}}{a_{l,0}}\right)^2$$

where a_l is the area per lipid, $a_{l,0}$ the equilibrium area per lipid, and K the elastic modulus. The membrane tension is therefore defined by

$$\Sigma = \frac{\partial F_{elastic}}{\partial a} = K\left(\frac{a_l - a_{l,0}}{a_{l,0}}\right)$$

If two lipid species are present in the membrane, phase separation will introduce a line tension term to the total free energy:

$$F_{line} = \sigma_{line} l$$

where l is the length of the interface. Finally, the energy of a bound colloid or surface is

$$F_{adh} = -e_{adh} A_{adh}$$

where e_{adh} is some energy per unit area and A_{adh} is the contact area.

3.2 CHARACTERIZATION OF MEMBRANE PROPERTIES

In order to compare experimental results and elastic theory with the results of our numerical simulations, we need to determine the values of the macroscopic parameters K, Σ, $a_{l,0}$, κ, and κ_G as a function of simulation parameters.

3.2.1 Elastic parameters from membrane stress profile

Estimation of several macroscopic parameters relies on measurement and manipulation of the stress difference across a flat membrane $[\Sigma_T - \Sigma_N](z)$. $\Sigma_T(z)$ and $\Sigma_N(z)$ are diagonal components of the stress tensor $\Sigma^{\alpha\beta}$, i.e.

$$\Sigma^{\alpha\beta} = \begin{pmatrix} \Sigma_T & 0 & 0 \\ 0 & \Sigma_T & 0 \\ 0 & 0 & \Sigma_N \end{pmatrix}$$

The tangential term $\Sigma_T(z)$ appears twice because the system is isotropic in the plane of the membrane, while the off diagonal terms are zero because the membrane has zero shear modulus, i.e. is a fluid. $\Sigma_N(z)$ is the component of the stress tensor normal to the membrane. We measure $\Sigma^{\alpha\beta}$ as in Goetz and Lipowsky.[14] The interfacial tension can then be calculated as the (numerical) integral of the stress profile:

$$\Sigma = \int_{-\infty}^{\infty} \left(\Sigma_T(z) - \Sigma_N(z)\right) dz$$

We measure Σ as a function of a_l for several values of the angle coefficient. The system is periodic with dimensions L_x, L_y, and L_z. The membrane spans the system in the x and y directions, for which the cross-sectional area of the system is $A_C = L_x L_y$. The area per lipid is defined as $a_l = 2A_C / N$ where N is the total number of lipids and the factor of 2 accounts for the two sides of the bilayer.

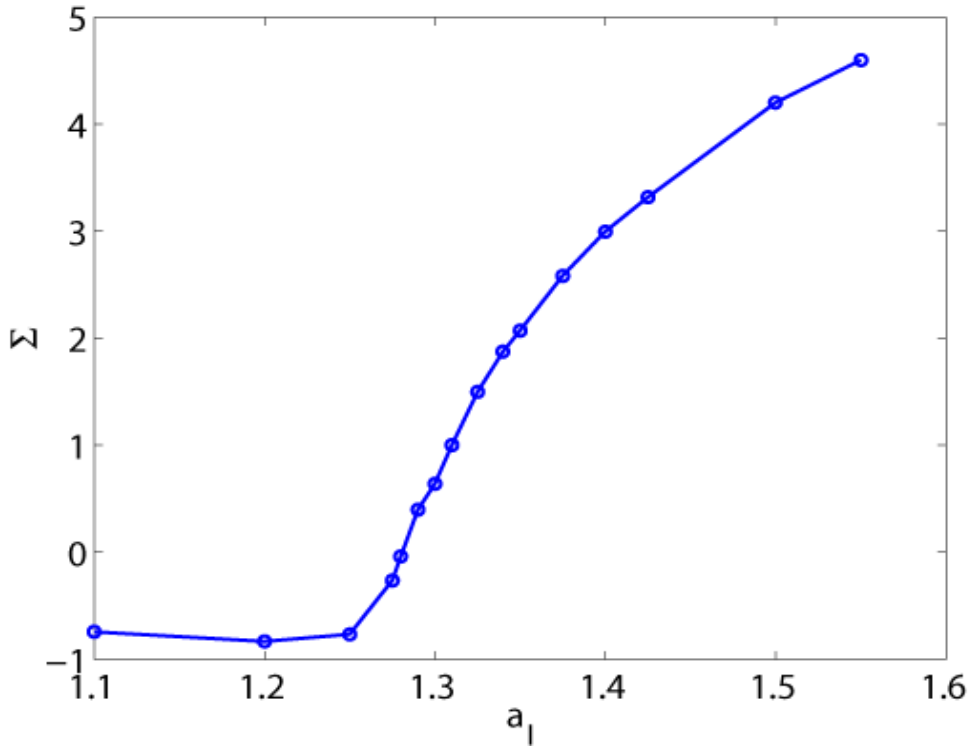

Figure 5 – Graph of tension versus area per lipid for an angle coefficient of 10

Obviously, $a_{l,0}$ can be determined from $\Sigma(a_{l,0}) = 0$, the tensionless state of the membrane. From a linear fit of $\Sigma(a_l)$ at low membrane tension, we find $K \approx 33.2 k_B T / r_c^2$. An analysis of thin elastic films shows that κ can be estimated as $\kappa = Kh^2/48$, where h is the membrane thickness, in good agreement with direct numerical[15] and experimental measurements.[16] Substituting in our value for *K*, we obtain $\kappa \approx 11 k_B T$ for our system.

From the tensionless state of the membrane, we can determine the Gaussian modulus κ_g as the integral of the second moment of the stress profile:[17]

$$\kappa_g = \int_{-\infty}^{\infty} z^2 \left(\Sigma_T(z) - \Sigma_N(z)\right) dz$$

We show κ_g as a function of angle coefficient K_{angle} below:

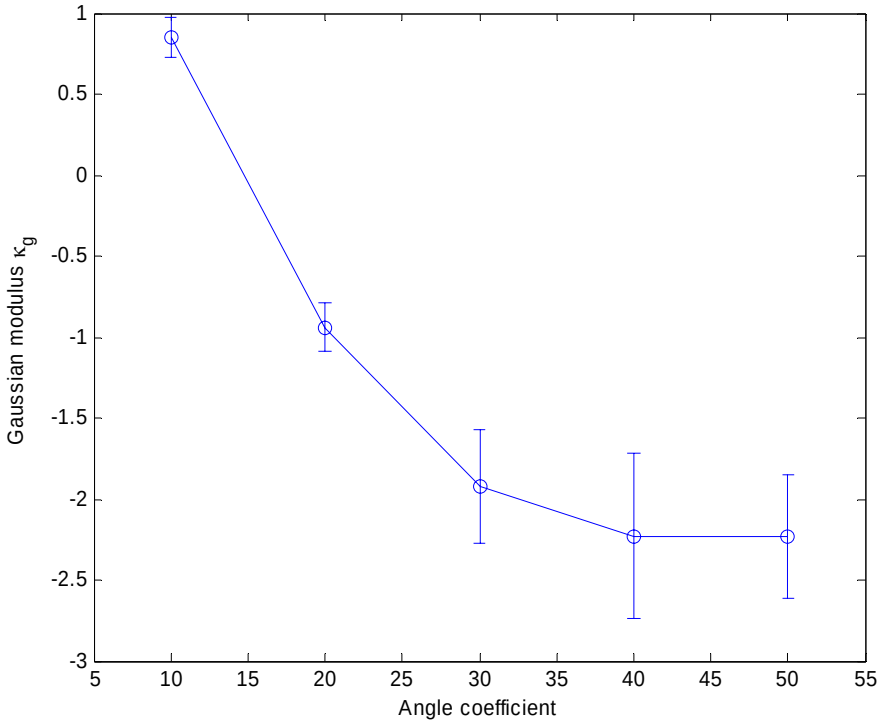

Figure 6 – Gaussian modulus as a function of angle coefficient

Note that we can construct lipids with both positive and negative values of κ_g. The former will favor saddle morphologies, the latter spherical morphologies.

Next we consider measurement of the line tension associated with a pore, σ_{edge}, or with an interface between two lipid species, σ_{int}. To determine σ_{edge}, we measure the stress tensor for a membrane in a periodic box that spans the box in the x direction and has free edges in the y direction, with z the coordinate normal to the membrane. The stress tensor is diagonal and has two components, Σ_X and Σ_Y, in the plane of the membrane. We measure the difference $(\Sigma_X - \Sigma_Y)$ and integrate in the y direction to determine a surface tension $\int_{-\infty}^{\infty}(\Sigma_X - \Sigma_Y)dy$. To convert to a line tension, we integrate in the z direction:

$$\sigma_{edge} = \int_{-\infty}^{\infty}\int_{-\infty}^{\infty}(\Sigma_X - \Sigma_Y)dydz$$

By this procedure, we determined the energy of a free edge to be $\sigma_{edge} \approx 4.9k_BT / r_c$.

Similarly, to obtain an interfacial tension σ_{int}, we have measure the stress tensor of a membrane that spans a periodic box in the x and y directions with a line interface normal to the y direction. We again integrate the stress difference to obtain the interfacial tension:

$$\sigma_{\text{int}} = \int_{-\infty}^{\infty}\int_{-\infty}^{\infty}(\Sigma_X - \Sigma_Y)dydz$$

We vary the line tension by varying the repulsion coefficient between the head groups of the two lipid species. σ_{int} is shown as a function of this DPD repulsion coefficient in the graph below:

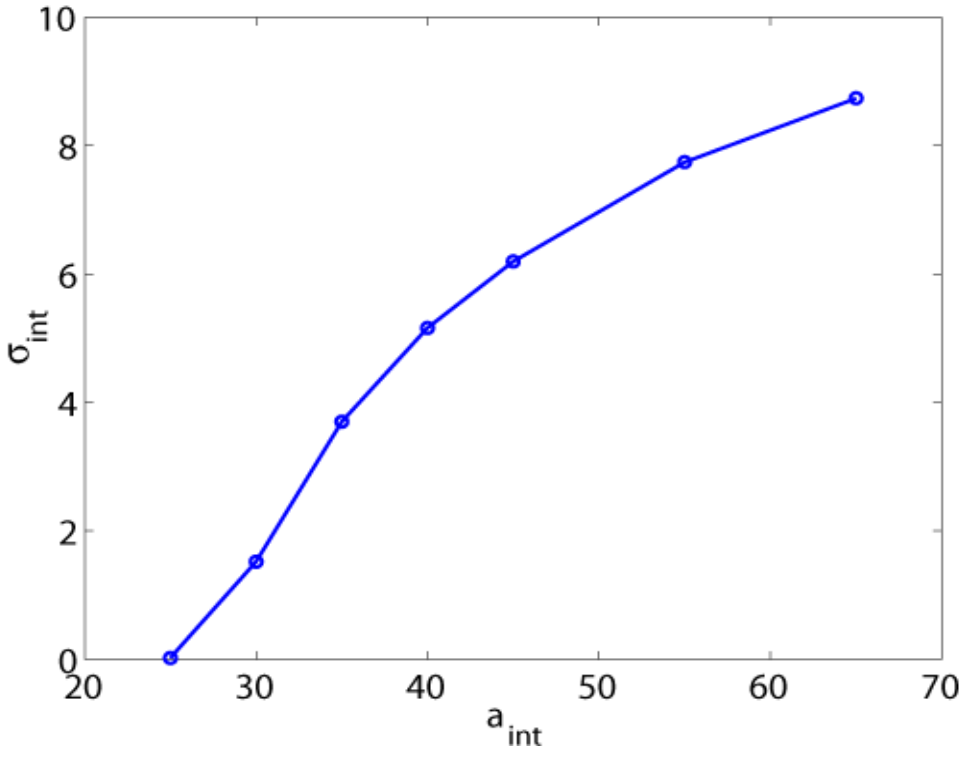

Figure 7 – Interfacial tension as a function of the head-head repulsion parameter for two lipid species

3.2.2 Estimation of adhesion energy

Adhesion energy e_{adh} arises in our simulations when we increase the repulsion coefficient between a solid surface or particle and solvent from $a_{PS} = 25$. It then becomes energetically advantageous for head groups in a lipid membrane, for which $a_{HP} = 25$, to make contact with the solid particle. To calculate e_{adh}, we set up a simulation box periodic in the x and y directioms, with solid walls normal to the z direction spanning the box. We fill the box with solvent, and initially set $a_{PS} = 25$. We measure the surface tension of the wall-solvent interface as e_{coated}. We then increase a_{PS} above 25 and measure the surface tension of the wall-solvent interface as $e_{uncoated}$. We can then determine the adhesion energy e_{adh} for this value of a_{PS} as

$$e_{adh} = e_{uncoated} - e_{coated}$$

In this manner, we vary a_{PS} over $30 \le a_{PS} \le 60$ and calculate e_{adh}. For this range of a_{PS}, we find e_{adh} to be on the order of $1 - 14 k_B T / r_c^2$. The results of these measurements are shown in the figure below:

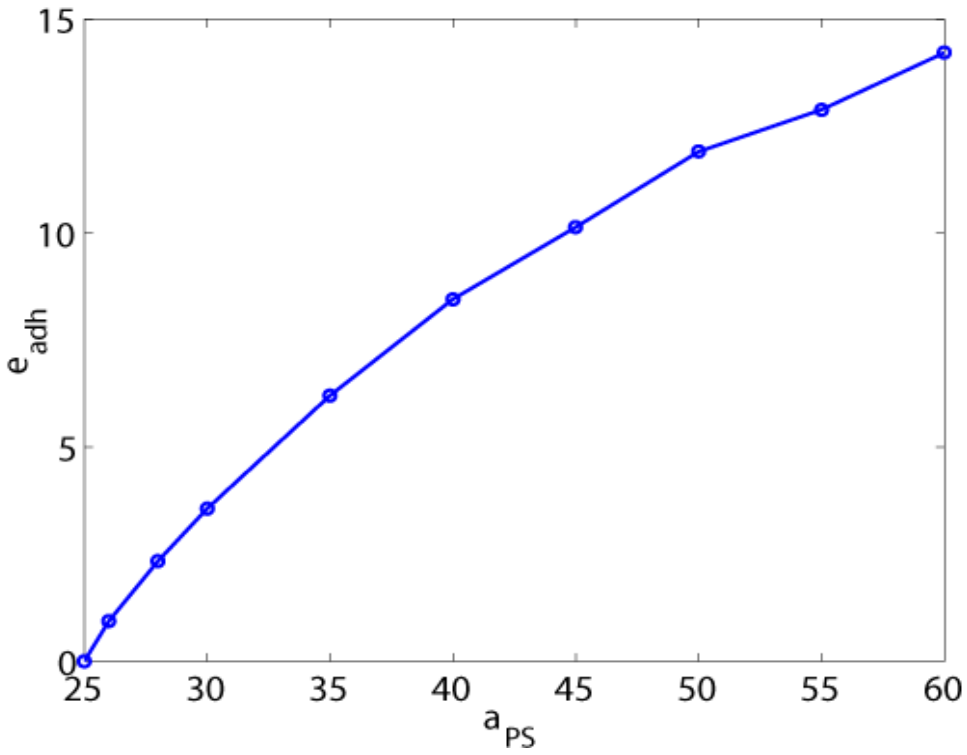

Figure 8 – Adhesion energy per unit area as a function of particle-solvent repulsion parameter a_{PS}

3.3 PREPARATION OF VESICLES

We prepare a simulation box that is periodic in the x and y directions and has solid walls normal to the z axis. Walls are constructed out of rigidly frozen, FCC close packed particles, oriented such that their (111) planes are normal to the z axis. The dimensions of the box are $L_x = 70r_c$, $L_y = 52r_c$, and $L_z = 70r_c$ between the parallel walls.

We form vesicles of radius $R = 15r_c$, as measured from the origin to the bilayer midplane, by randomly distributing lipids across the inner and outer monolayers on a spherical surface. We fix membrane thickness $h = 3r_c$, calculating the number of inner lipids n_{inner} and outer lipids

n_{outer} such that both leaflets have area per lipid $a_l = 1.35 r_c^2$. At this value the vesicle has zero surface tension; $a_{l,0}$ is determined as in Section III. Lipid architecture is as described in Section II, with $K_{angle} = 20$ and $K_{bond} = 64$. Furthermore, we tether the vesicle to the center of the simulation box with a harmonic bond potential

$$E_{tether} = K_{tether}(r - r_0)^2$$

where $K_{tether} = 50$, r is the center of mass of all lipids, and $r_0 = 0$. The spring force is equally distributed across all lipid beads.

We solvate the box such that $\rho = 3/r_c^3$, with N solvent particles distributed in the vesicle interior.

In order to create multicomponent vesicles, we designate the lipids between the angles ϕ_0 and $\phi = \pi$ as type 2, where $\pi/2 \le \phi_0 \le \pi$, with the remaining lipids designated as type 1. In this manner, we create a circular, minority domain with area

$$A_d = 2\pi R^2[1 + \cos(\phi_0)]$$

We define the relative domain size as

$$a = A_d / 4\pi R^2$$

With the vesicle constructed, we allow the system to relax and equilibrate for several thousand timesteps.

Solvation of the vesicle interior by N particles can introduce a surface tension if $N > N_{eq}$. In order to determine N_{eq}, we create a small hole in a single component vesicle and allow the system to equilibrate. The vesicle exchanges interior solvent with the exterior fluid

until interior and exterior pressures are equalized, thereafter closing. In this fashion we determined $N_{eq} \approx 84000$. We define reduced volume V^* by

$$V^* = N / N_{eq}$$

For $V^* < 1$, a vesicle is flaccid and has excess area in the lipid membrane. Vesicles with $V^* > 1$ are tense, owing to excess interior pressure.

3.4 EQUILIBRIUM CONFORMATIONS OF SINGLE COMPONENT MEMBRANES

The shape of a single component vesicle is primarily determined by reduced volume V^*. We construct vesicles for various values of V^*. Figure 9 shows two such vesicles. At $V^* = 1$, as in Figure 9a, a single component vesicle is spherical; at $V^* = 0.86$, as in Figure 9b, it is an oblate ellipsoid.

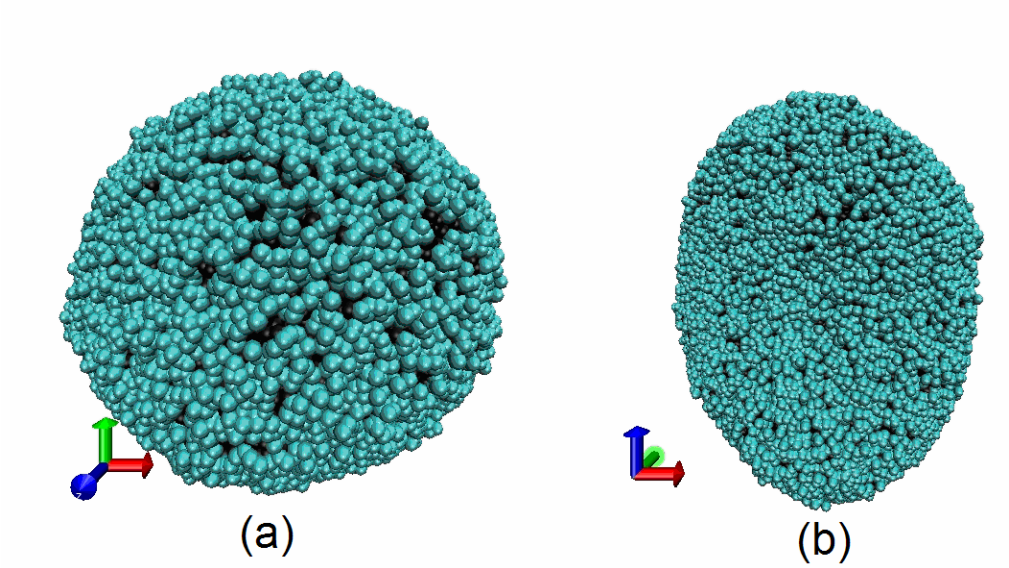

Figure 9 – Equilibrium conformations of a single component vesicle. Figure (a) shows a spherical homogeneous vesicle with V* = 1. Figure (b) shows an oblate ellipsoid with V* = 0.86.

3.5 EQUILIBRIUM CONFORMATIONS OF MULTICOMPONENT MEMBRANES

The equilibrium shape of a multicomponent vesicle is determined by the balance of stretching, bending and line energies. Line energy will favor budding, which is the mushroom-like protrusion of the minority domain into the space surrounding the vesicle, as it reduces the length of the domain interface. On the other hand, budding requires the introduction of bud curvature, and therefore an increase in bending energy. The interplay of these energies determines the radius of the neck connecting the budded domain to the vesicle bulk. The ratio of line and bending energy strengths can be nondimensionalized as:

$$\sigma^* = \sigma_{\text{int}} R / \kappa$$

Introducing a second lipid species, then, introduces two additional nondimensional parameters. σ^*, a and V^* determine the equilibrium conformation of a multicomponent

membrane. We measure κ and σ_{int} as described in Section III. By varying σ^*, a, and V^* by varying $a_{H_1H_2} = a_{T_1T_2}$, ϕ_0, and N, we can simulate equilibrium vesicle shapes.

In order to verify our simulations, we compare the equilibrium shapes to the free energy minimizing shapes calculated by Julicher and Lipowsky.[4] Figure 8 of Julicher shows equilibrium vesicle shapes for $\sigma^* = 0.9$, $a = 0.1$, and varying V^*. Varying V^* accordingly, we observe good agreement with the predicted shapes:

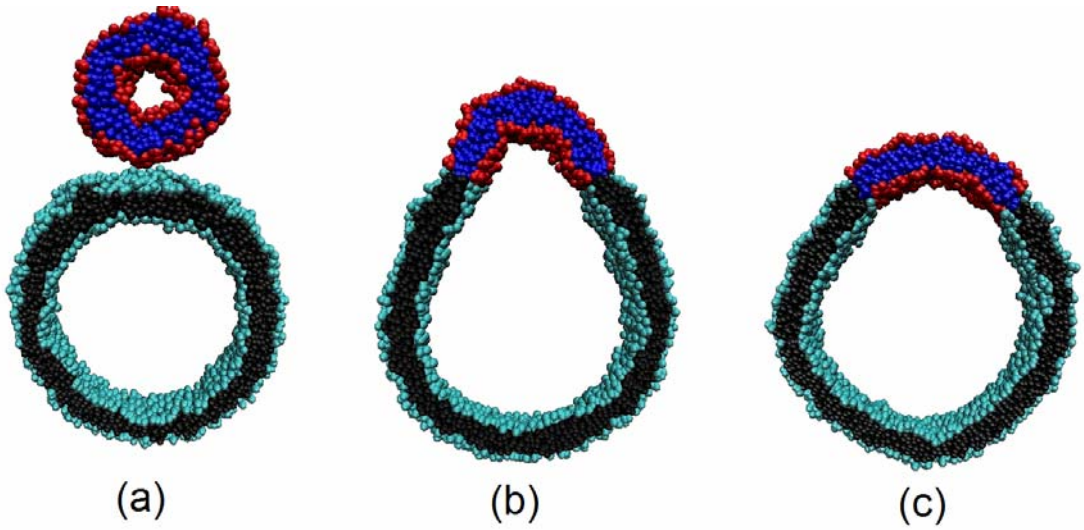

Figure 10 – Equilibrium conformations of multicomponent vesicles with a = 0.1, σ^* = 0.9, and varying V*. For (a), V* = 0.98; for (b), V* = 0.95; for (c), V* = 0.9.

Although we find that the minority domain pinches off for higher than the predicted V^*, this is attributable to the finite thickness of the membrane, which makes the diameter of the neck less than it would be for an infinitesimally thin membrane.

We next set $a = 0.23$ and vary σ^* and V^*. We find that for each V^*, there is a critical value σ^*_{crit} for which no stable bud exists. (Figure 11) The minority domain buds and pinches

off, with the neck diameter constricting to nearly zero, at which point the bud detaches as a daughter vesicle. For $0.9 \le V^* \le 0.92$, the initial vesicle shape is nearly spherical before line tension is turned on, and the vesicle cannot deform to create a bud. Accordingly, increasing σ^* causes the vesicle to tear along the domain interface, which remains open without complete detachment of the minority domain.

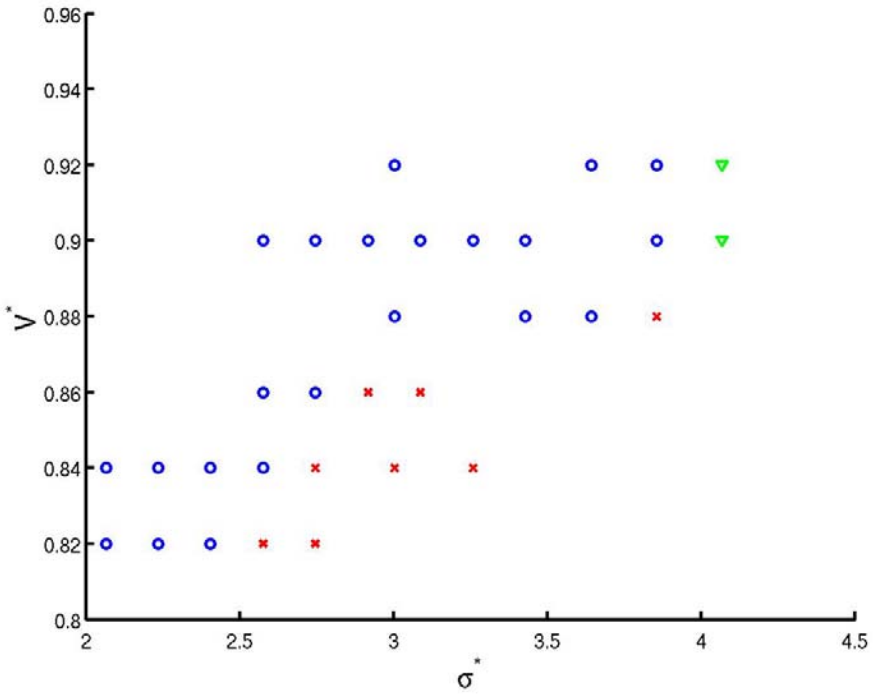

Figure 11 – Phase diagram of equilibrium conformations of multicomponent membranes for V* vs. σ^***.** Blue circles indicate stable budding, red crosses unstable buds that pinch off, and green triangles ripping at the domain interface.

4.0 VESICLES UNDER SHEAR

4.1 INTRODUCTION

Single component vesicles in shear have already seen considerable study. Their behavior is known to depend on the viscosity contrast between the membrane and the surrounding fluid, which determines whether vesicle behavior is solidlike or liquidlike, i.e. whether the vesicle undergoes tumbling or tank-treading. The behavior of multicomponent budded vesicles in shear, however, has hitherto not been examined. We find that similar results obtain for multicomponent vesicles as for single component vesicles, with the ratio of shear to line tension playing the role of the viscosity contrast in determining vesicle behavior. However, we also find that shear can drive morphological and even topological change not seen in single component vesicles: flattening and pinch-off of the budded minority domain. We work out the phase diagram of such morphological change and determine the conditions for pinch-off, providing guidelines for vesicle design for drug delivery.

A solidlike single component vesicle is akin to a rigid ellipsoid. The rotational motion of a rigid ellipsoid in shear was first studied by Jeffrey, whose analytical theory[18] has been corroborated by more recent experimental[19] and numerical[20,21] studies. In shear, a rigid ellipsoid will align its major axis parallel to the shear plane. Since there is no stable, steady state solution to the Navier-Stokes equations for a stationary ellipsoid that satisfies the no-slip boundary

condition, such an ellipsoid must rotate around its minor axis, which is normal to the shear plane. A prolate vesicle, for instance, must flip end over end.

In tank-treading vesicles, on the other hand, viscous stresses are sufficiently strong to drive tangential flow of the membrane. The no-slip boundary condition for solids does not apply, and the vesicle behaves like a liquid droplet, maintaining a fixed angle of orientation with the direction of flow as the membrane fluid circulates around the vesicle body.[22]

In a budded multicomponent vesicle, the domain line tension can play the same role as the viscosity contrast in determining whether the vesicle undergoes tumbling or tank-treading. If the ratio of shear to line tension is small, shear is insufficient to increase the contact length and deform the vesicle into the ellipsoidal shape necessary for tank-treading; tumbling must occur.

Furthermore, shear forces can drive morphological change in budded multicomponent vesicles. From the familiar decomposition of simple shear into rotational and elongation components, (Figure 12) one can see that the elongational component can either promote flattening or pinch-off, depending on the bud position. If the angle of orientation of the vesicle is sufficiently small and the bud is at the vesicle tip, then the elongational component is mainly parallel to the axis connecting the vesicle body and the bud. If, on the other hand, the bud is located in the elongated region of the vesicle, then the elongational component is mainly perpendicular to this axis. (Figure 13) Bud circulation caused by the rotational component allows the bud to experience both flow environments, and the bud can be driven to either pinch-off or flatten. (Figure 14)

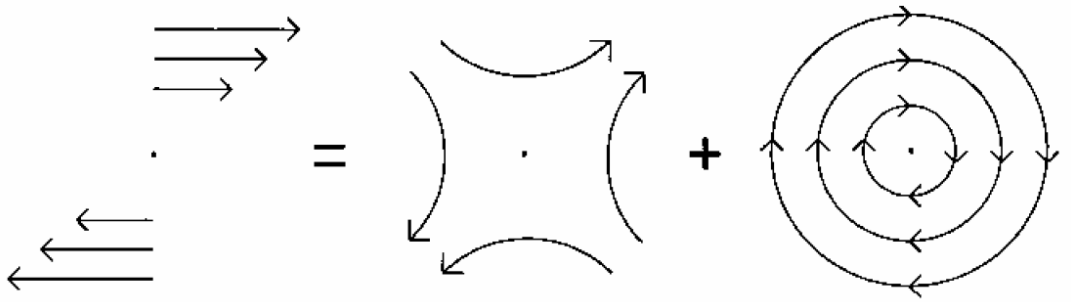

Figure 12 – Decomposition of simple shear into elongational and rotational components

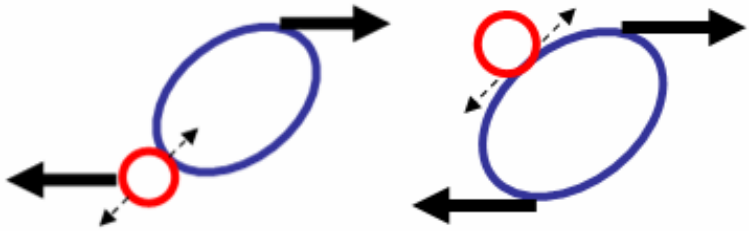

Figure 13 – The effect of the elongational component of simple shear on a budded domain depends on the bud position

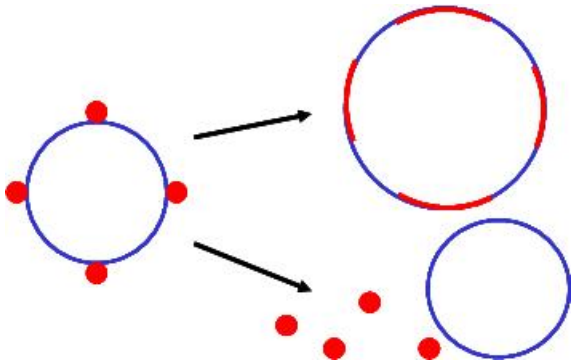

Figure 14 – Alternative pathways for a budded vesicle in shear

Whether the vesicle undergoes such a morphological change is determined by the size of the energy barriers for pinch-off and flattening, relative to the size of the shear force. For flattening, the barrier is the difference in interface length between the budded state and the

flattened state, multiplied by the interfacial tension. For pinch-off, the energy barrier is the stretching energy associated with the reduction of the neck diameter.

Using DPD, we investigate multicomponent vesicles in shear flow, first examining the tumbling to tank-treading transition with contrast γ^* / σ^*, and thereafter examining the effect of shear on the morphology of the budded domain. Via construction of a γ^* vs. σ^* phase diagram, we illuminate the conditions for pinch off and vesiculation.

4.2 PREPARATION OF VESICLES

Vesicles are prepared as described in Section 3.4. We impose the bounceback condition discussed in Section 2.2 to ensure that no solvent particles penetrate the walls. We designate x the flow direction and y the transverse direction, with $L_x = 70 r_c$, $L_y = 52 r_c$, and $L_z = 70 r_c$ between the parallel walls.

We allow the vesicles to equilibrate for several thousand time steps before turning on shear. Shear $u = (\gamma z, 0, 0)$ is imposed through motion of the parallel walls.

4.3 DIMENSIONLESS PARAMETERS AND RELATION TO EXPERIMENT

As discussed in Section III, the equilibrium conformation of a multicomponent vesicles is determined by the balance of line, bending, and stretching energies, or the dimensionless

parameters σ^*, a, and V^*. For our shear simulations, we choose to fix $a = 0.23$ and $V^* = 0.86$. Shear introduces another force in the system. The force of shear is approximately

$$f_{shear} \approx \gamma \mu R^2$$

where μ is the fluid viscosity. From our chosen DPD parameters, $\mu \approx 0.9 m_{DPD} / r_c \tau_{DPD}$.[11] We define a dimensionless shear rate as

$$\gamma^* \approx \gamma \mu R^3 / \kappa$$

Based on the values of σ_{int} and κ calculated in Section III, we determine that our simulations lie in the range of $\sigma^* \approx 2-5$ and $\gamma^* \approx 4-8$. For a mixed lipid membrane vesicle, $\kappa \approx 10^{-19} J$ and $\sigma \approx 10^{-12} J/m$, the value of σ^* agrees well with our simulations when $R \approx 0.5 - 2 \mu m$.[3,16] By comparing values of γ^* and taking $\mu = 0.001 Pa \cdot s$ for water, we find our simulations are equivalent to $\gamma^* = 10^4 / s$ for $R \approx 0.5 \mu m$ or to $\gamma^* = 10^2 / s$ for $R \approx 2 \mu m$. These are realistic shear rates for flow in a microchannel.[22]

4.4 RESULTS AND DISCUSSION

We first examine the tumbling-to-tank treading transition with the ratio γ^* / σ^*. To save computation time, we prepare a system of size $L_x = 48 r_c$, $L_y = 40 r_c$, and $L_z = 50 r_c$. From previous work on ellipsoidal particles, we would expect that tumbling would result from any initial orientation relative to the flow field. To test this prediction, we simulate the response of a budded vesicle whose major axis is initially perpendicular to the shear plane in low γ^* / σ^* flow ($\sigma^* = 2.15$ and $\gamma^* = 2.0$). We find that the vesicle orients its major axis to the flow plane in

approximately the time for a single rotation, tumbling such that the bud and vesicle body repeatedly flip over each other. Increasing the contrast γ^* / σ^* -- the shear analogue of viscosity contrast – we find that tank-treading does indeed occur at high γ^* / σ^*.

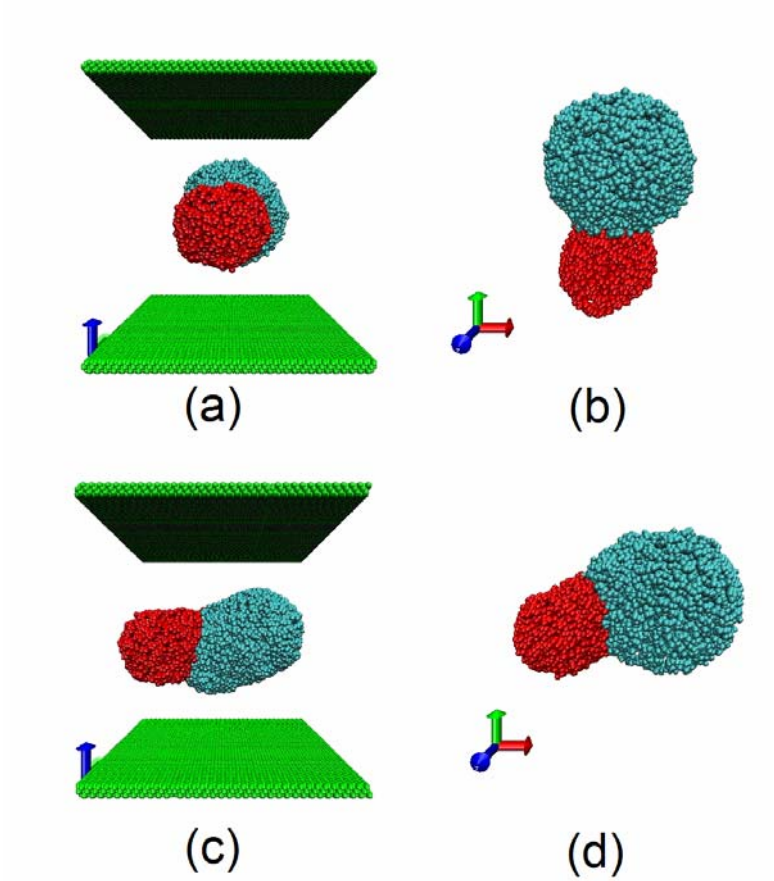

Figure 15 -- Shear-driven rotation of a budded vesicle whose major axis is initially perpendicular to the flow plane. V* = 0.86, a = 0.275, σ* = 2.15, and γ* = 2.0. Images (a) and (b) show the initial configuration of the vesicle from a side and top view, respectively; image (b) omits the walls. Images (c) and (d) show the vesicle after one complete rotation of the bud about the body, from the same perspectives as (a) and (b). The upper wall is moved to the right and the lower wall to the left in all images.

Knowing that vesicles align with shear flow, we investigate the effect of shear on the budded domain. We find that three major behaviors accompany the introduction of shear:

1. The bud remains closed and circulates periodically around the vesicle
2. The bud is stretched open, and the entire vesicle undergoes tank treading
3. After migrating to the vesicle tip, the bud detaches from the body in a smooth pinch-off process

Additionally, behavior intermediate between cases 1 and 2 is possible; the budded domain may only partially flatten and circulate around the vesicle. As discussed in the introduction, the qualitatively different behaviors are due to the multiple roles shear can play, depending on the bud location. By way of example, a set of parameters giving very weak shear, and therefore behavior 1, is $V^* = 0.86$, $a = 0.23$, $\sigma^* = 2.15$ and $\gamma^* = 3.91$. In Figure 16, we see the vesicle body is elongated, but the bud is relatively undeformed. It remains budded as it circulates around the vesicle.

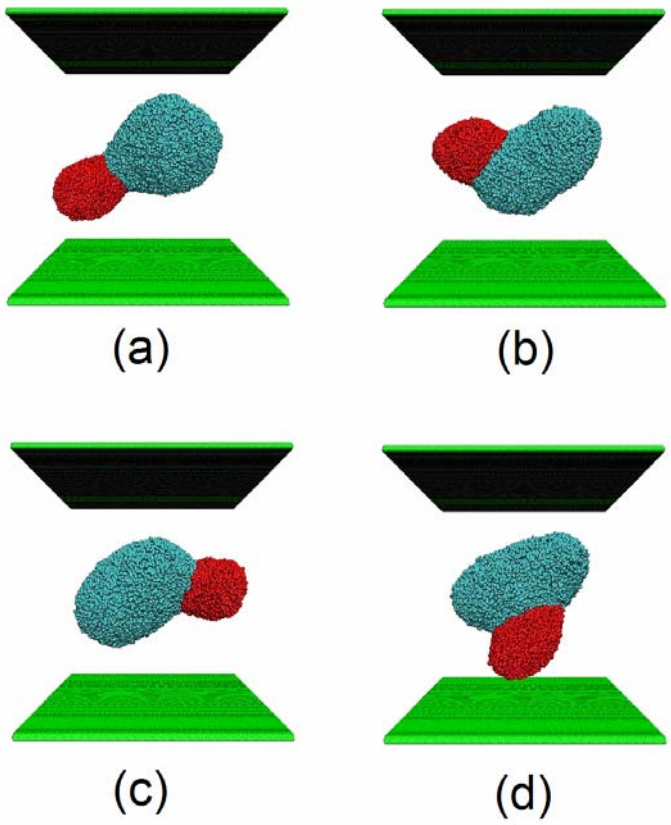

Figure 16 – Circulation of an undeformed bud. V* = 0.86, a = 0.23, σ* = 2.15, and γ* = 3.91.

When shear is increased to $\gamma^* = 6.52$ for the same vesicle, shear forces overcome line tension and flatten the domain when it arrives in the central region of the vesicle. (Figure 17c) It is in this region that elongational forces act to flatten the domain. The result is a prolate shape, much like that seen for single component vesicles in shear. The flattened domain is then convected by the tank-treading motion of the vesicle, not changing significantly as it passes the vesicle tips. (Figure 17d)

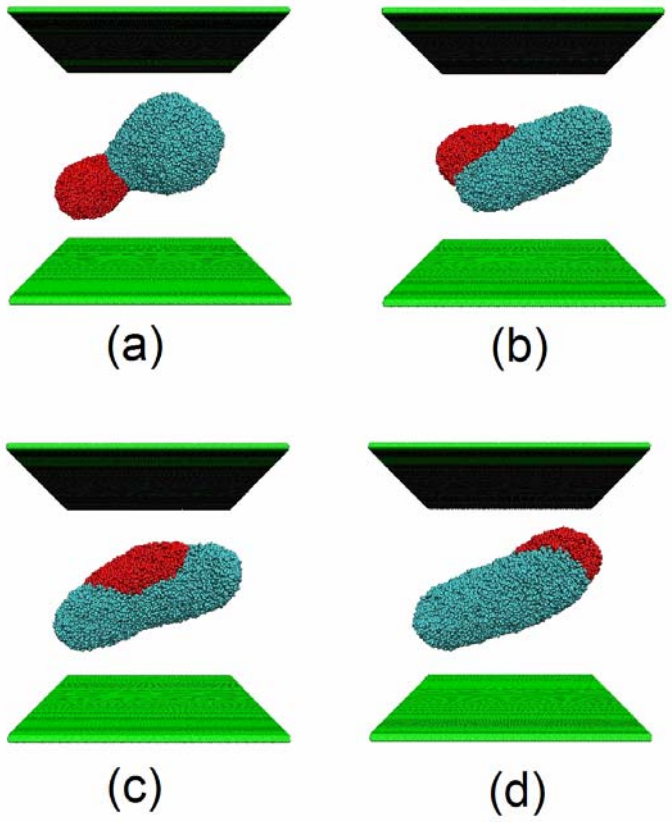

Figure 17 – Flattening of a budded domain for V* = 0.86, a = 0.23, σ* = 2.15, and γ* = 6.52. The bud flattens when it arrives in the central region of the vesicle, and the vesicle is deformed to a prolate shape.

Finally, with high line tension ($\sigma^* = 2.75$), even weak flow ($\gamma^* = 3.91$) is sufficient to a drive a normally stably budded domain over the energy barrier for vesiculation. Figure 18 shows the time sequence for shear-driven pinch off for this vesicle. When the bud arrives at the vesicle tip, it becomes "stuck," and is stretched away from the vesicle body by the shear force. The neck constricts, leading eventually to pinch off. Examination of the pinch off event reveals it is initiated by the creation of a pore at the domain interface. To ensure that pinch off does not depend on the initial orientation of the bud, we simulated this set of parameters for the initial orientations in Figure 16a and Figure 17a as well as that in Figure 18a. We did not see any

dependence on the initial orientation; the outcome is not due to the initial placement of the bud near the vesicle tip.

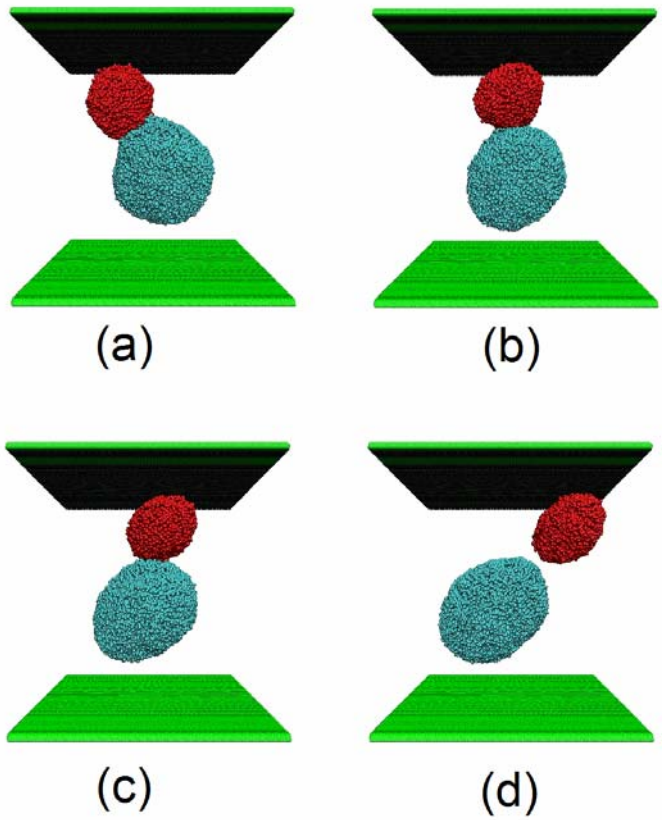

Figure 18 – Pinch-off of a budded domain for V* = 0.86, a = 0.23, σ* = 2.75, and γ* = 3.91. The bud migrates to the vesicle tip, where the pinch-off process occurs.

We work out a phase diagram for varying σ^* and γ^*, allowing the vesicle to equilibrate before turning on shear. (Figure 19) For small line tension $\sigma^* = 2.15$, we observe only a transition from circulation to flattening, while for large line tension we find that the budded domain pinched off for sufficiently high shear rate γ^*.

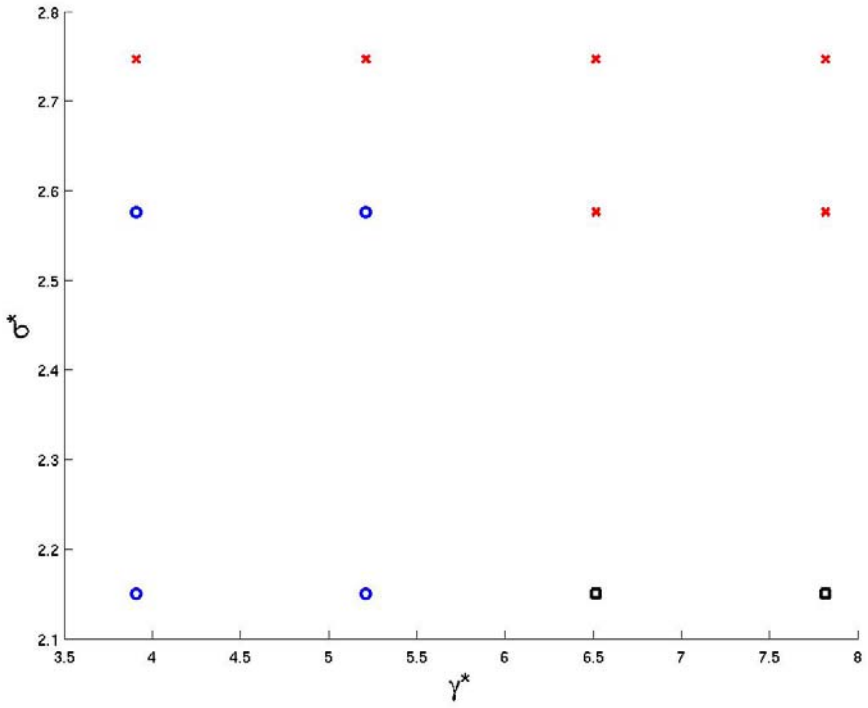

Figure 19 – Phase diagram of vesicle behavior in shear flow for σ* vs. γ*. Blue circles indicate a stable, circulating bud; black squares indicate bud flattening; and red crosses indicate bud pinch-off.

4.5 CONCLUSIONS

We examine the behavior of multicomponent budded vesicles in shear flow, finding that γ^* / σ^* can play the same role as the viscosity contrast in determining whether membrane behavior is solidlike or liquidlike, i.e. whether the vesicle tumbles or undergoes tank-treading. Budded vesicles are observed to orient their major axes in the flow plane. Furthermore, we examined the effect of imposed shear on bud morphology, finding shear can drive morphological and topological changes in the vesicle. We probe the conditions for domain flattening and domain pinch off, and explain vesicle behavior on the basis of membrane energetics and the

decomposition of simple shear. These results provide guidelines for the design of "packet" release in drug delivery. Vesicles could be tailored to release "packets" in specific flow regions, e.g. specific regions of the human bloodstream.

5.0 FISSION OF CATENOID NECKS

Increasingly, physical scientists are turning their attention to cellular biology, both to understand biology on the basis of physical principles and for inspiration for the design of synthetic systems. Phagocytosis, the uptake of particles by the cell membrane, is one cell phenomenon that could be modeled physically and mimicked by synthetic soft materials. Understanding of the mechanism of biological phagocytosis would greatly aid targeted drug delivery. Moreover, the toxicity of nanoparticle contaminants has recently been a subject of controversy. Synthetic vesicles designed for selective biomimetic phagocytosis could remove such contaminants from the environment.

In previous work, Smith *et al*. studied the uptake of particles of radius on the order of the membrane thickness, illuminating the conditions for complete wrapping and phagocytosis.[24] The length scale of that study, however, limited examination of the mechanism of pore creation and neck scission. Numerically and analytically, we model the fission of *large* encapsulated particles via pore nucleation and growth in the narrow neck region. We delineate the physical conditions for pore nucleation and growth, providing principles for the physical operation of biological cells and criteria for the design of synthetic vesicles that take up large colloidal particles. Secondly, since such necks are formed by large phase segregated domains, e.g. in peanut-shaped vesicles composed of two types of lipids, we examine fission driven by a domain interface located in the neck.

Whereas the work of Smith *et al*. was largely exploratory, we calculate pore energetics on the basis of continuum elastic theory, considering both membranes with an interface between two lipid species, and membranes in contact with an adhesive particle. For the purposes of comparison, we also consider the energetics of a simpler case, a homogeneous membrane with a neck. For all cases we determine the conditions for pore stability and the height of the energy barrier for pore nucleation.

Using Dissipative Particle Dynamics (DPD), we model fission in heterogeneous membranes and in adhesive particle/membrane systems. Macroscopic elastic parameters were calculated as a function of simulation parameters in Section 3, allowing us to compare the statistics of our simulations with the statistics predicted by elastic theory.

Accordingly, we first develop the analytical theory, thereafter discussing our numerical methodology. Finally, we present and discuss preliminary numerical results. Ultimately, we aim to compare them to the predictions made by the elastic theory.

5.1 PORE ENERGETICS

Common to the fission of budded domains and of encapsulated particles is the role of pore growth in the membrane neck. In the initial stage of large particle phagocytosis, the particle is wrapped by the membrane, with the degree of envelopment determined by the balance of adhesion and stretching energies. Previous analytical studies have worked out the phase diagram for large colloid wrapping and the conditions for complete envelopment.[6] When completely enveloped, the encapsulated particle is connected to the bulk membrane by a narrow neck. Likewise, after phase segregation and budding of a large domain, the bulk and minority domains

are also connected by such a neck. Given the length scale of the system, curvature energy to wrap the particle or form the budded domain is negligible and the neck can be considered to connect two flat membranes. Neck radius is then determined by the balance of line or adhesion energy, which favor constriction, and stretching energy, which promotes neck expansion.

This neck can reduce its curvature energy by relaxing to a saddle shape, acquiring principal curvatures of opposite sign, and therefore low mean curvature. The catenoid, the surface of revolution of the caternary, has exactly zero mean curvature. Like the bicontinuous cubic phase, it is a minimal surface, and it approximately describes the shape of the membrane in the neck region. The catenoid is completely characterized by one parameter, the neck radius.

With formation of a catenoid neck, no further smooth deformation of the membrane promotes endocytosis. Fission must proceed through nucleation and growth of a pore. If the neck is sufficiently small, little of the interior solvent or cytosol will be lost to the environment.[25]

Pore creation is favored by Gaussian energy, as well as either adhesion or interfacial energy, and opposed by edge energy. Gaussian energy is normally neglected in calculations of equilibrium membrane conformations. According to the Gauss-Bonnet theorem, Gaussian energy is unchanged for any deformation of a surface with fixed genus and boundaries. For catenoids and other unbounded genus zero surfaces, Gaussian energy is given by

$$E_{gauss} = -4\pi\kappa_g$$

In the catenoid most of this Gaussian energy is concentrated in the narrow neck region. Since the creation of a pore constitutes a change in genus and boundaries, a catenoid can significantly reduce Gaussian energy via creation of a pore in the neck region.

We first develop the theory for pore growth driven only by Gaussian energy, thereafter considering pore growth with adhesion and pore growth with an interface.

5.2 PORE ENERGETICS WITHOUT ADHESION

When the neck relaxes to a catenoid, the curvature term in the usual Helfrich expression of the membrane free energy becomes zero, leaving only stretching and Gaussian curvature energies:

$$F = \int dA\left[f_a + \kappa_G C_1 C_2 \right]$$

Nucleation and growth of a pore introduces an edge energy while reducing Gaussian energy. Neglecting stretching energy, we take the free energy of a pore as the sum of Gaussian and edge energies:

$$\Delta E = \Delta E_{gaussian} + \Delta E_{edge}$$

In this section we derive an expression for the free energy of a pore in a catenoid and determine the conditions for pore stability.

5.2.1 Gaussian energy

Consider a pore of height Δh and a width subtended by angle $\Delta\theta$:

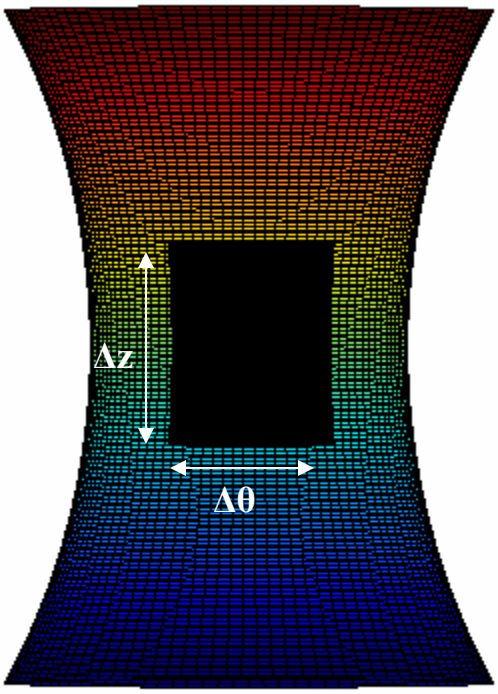

Figure 20 – System considered by elastic theory

To obtain the change in Gaussian energy, one must integrate the Gaussian curvature over the pore area:

$$\Delta E_{gauss} = -\int_{-\Delta z/2}^{\Delta z/2}\int_{-\Delta\theta/2}^{\Delta\theta/2} \kappa_g c_1 c_2 r d\theta dz$$

The catenary is a plane curve described by the equation $r(z) = R\cosh(z/R)$, where R is the radius at $z = 0$, the narrowest point of the neck. We take the first principal curvature to be that of the circle of revolution: $c_1(z) = 1/r(z)$. The second principal curvature is simply that of the $r(z)$ plane curve: $c_2 = \dfrac{-r''(z)}{(1+r'(z)^2)^{3/2}}$. We therefore have

$$\Delta E_{gauss} = \kappa_g(\Delta\theta)\int_{-\Delta z/2}^{\Delta z/2}(1/R)\sec h^2(z/R)dz$$

$$\Delta E_{gauss} = 2\kappa_g(\Delta\theta)\tanh(\Delta z/2R)$$

We define dimensionless Gaussian modulus κ_g^* as $\kappa_g^* = \dfrac{\kappa_g}{\sigma_{edge}R}$, the dimensionless energy ΔE^* as $\Delta E^* = \dfrac{\Delta E}{2\sigma_{edge}R}$, and dimensionless height Δz^* as $\Delta z^* = \Delta z / R$. The nondimensionalized Gaussian energy is then

$$\Delta E^*_{gauss} = \kappa_g^*(\Delta\theta)\tanh(\Delta z^*/2)$$

5.2.2 Edge energy

If σ_{edge} is the line tension of a pore edge, we can write the edge energy as

$$\Delta E_{edge} = \sigma_{edge}\oint dl$$

The two horizontal and two vertical edges comprise the path of the integral:

$$\Delta E_{edge} = \sigma_{edge}\left[(\Delta\theta)r(\Delta z/2) + (\Delta\theta)r(-\Delta z/2) + 2\int_{-\Delta z/2}^{\Delta z/2}\sqrt{1+r'(z)^2}dz\right]$$

$$\Delta E_{edge} = 2\sigma_{edge}\left[(\Delta\theta)R\cosh(\Delta z/2R) + 2R\sinh(\Delta z/2R)\right]$$

Nondimensionalizing as before, we have

$$\Delta E_{edge}* = \left[(\Delta\theta)\cosh(\Delta z*/2) + 2\sinh(\Delta z*/2)\right]$$

The free energy of the pore is therefore

$$\Delta E^* = \kappa_G{}^* (\Delta\theta)\tanh(\Delta z^*/2) + \left[(\Delta\theta)\cosh(\Delta z^*/2) + 2\sinh(\Delta z^*/2)\right]$$

5.3 EQUILIBRIUM PORE WITHOUT ADHESION

For a pore to be in equilibrium, we require $\frac{\partial \Delta E^*}{\partial \Delta\theta} = 0$ and $\frac{\partial \Delta E^*}{\partial \Delta z^*} = 0$. The first criterion yields

$$\kappa_g^* \tanh(\Delta z_{eq}^*/2) + \cosh(\Delta z_{eq}^*/2) = 0$$

$$\sinh^2(\Delta z_{eq}^*/2) + \kappa_g^* \sinh(\Delta z_{eq}^*/2) + 1 = 0$$

Solving this quadratic equation for Δz_{eq}^*, we have

$$\Delta z_{eq}^* = 2\,\text{arcsinh}\left(\frac{-\kappa_g^* \pm \sqrt{\kappa_g^{*} - 4}}{2}\right)$$

For $\kappa_g^* > -2$, the values of Δz_{eq}^* are complex; $\kappa_g^* = -2$ is a bifurcation point and two real equilibrium solutions exist for $\kappa_g^* < -2$. Equilibrium values of $\Delta\theta$ are determined by the second equilibrium criterion:

$$(1/2)\kappa_g^*(\Delta\theta_{eq})\sec h^2(\Delta z_{eq}^*/2) + \Delta\theta_{eq}/2\sinh(\Delta z_{eq}^*/2) + 2\cosh(\Delta z_{eq}^*/2) = 0$$

$$\Delta\theta_{eq} = \frac{2\cosh(\Delta z_{eq}/2)}{-\kappa_g{}^* \sec h^2(\Delta z_{eq}^*/2) - \sinh(\Delta z_{eq}^*/2)}$$

Substituting this equation into the equation for Δz_{eq}^* determines $\Delta\theta_{eq}$.

Figures 20 and 21 show Δz_{eq}^* and $\Delta\theta_{eq}$ as functions of κ_g^*, where solid (green) lines represent stable equilibria and dashed (blue) lines represent unstable equilbria. For $\kappa_g^* > -2$ no

physical solutions exist. For $\kappa_g^* < -2$, the only physical solutions are the set of stable equilibria, as the unstable equilibria have negative $\Delta\theta_{eq}$.

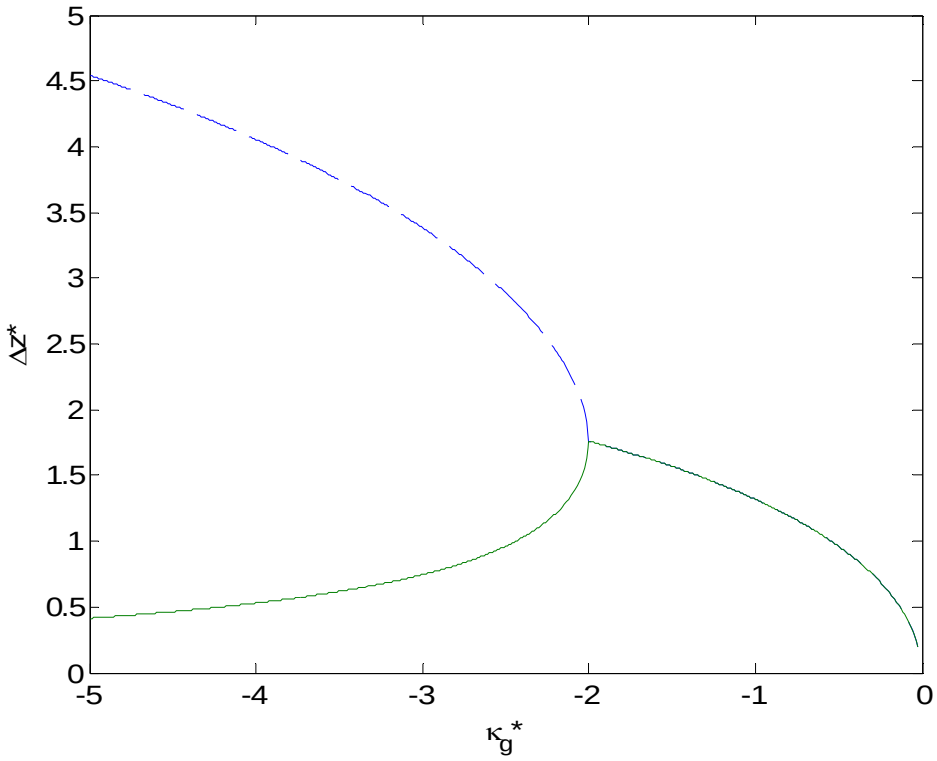

Figure 21 – Equilibrium Δz* for pores in a homogeneous neck. Real solutions emerge in a bifurcation at $\kappa_g^* = -2$; green is stable/negative root and blue is unstable/positive root.

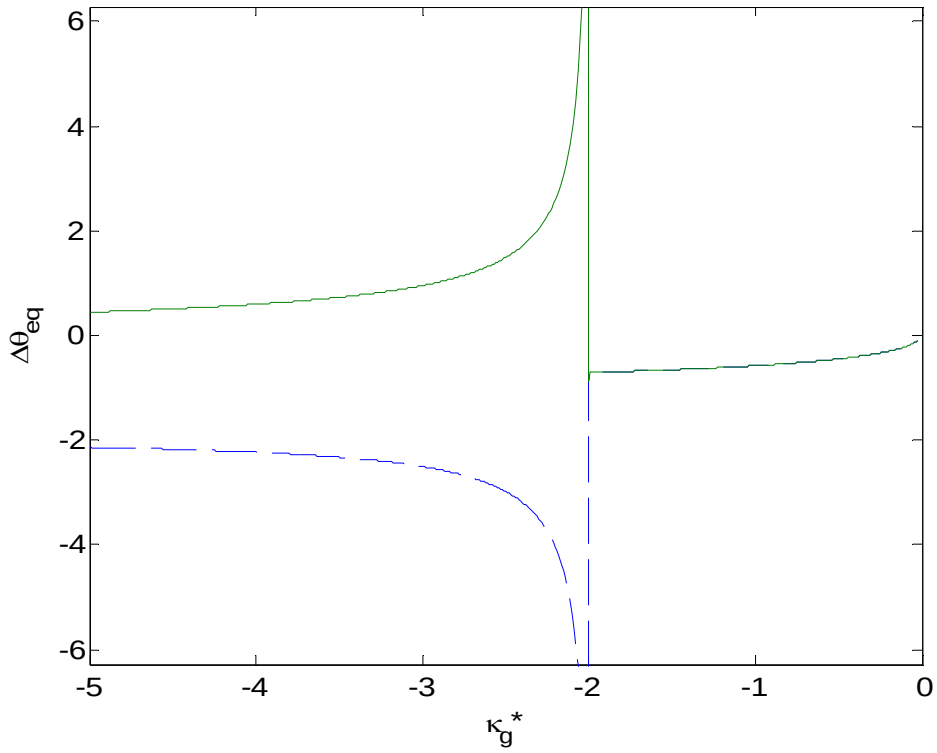

Figure 22 -- Equilibrium Δθ* for pores in a homogeneous neck. Real solutions emerge in a bifurcation at $\kappa_g^* = -2$; green is the stable root and blue is the unstable root.

When the energetic landscapes are plotted for various values of κ_g^*, it can clearly be seen that the equilibrium pores are saddle points. The saddle point energy is plotted in Figure 3 as a function of κ_g^*, giving the size of the energy barrier to pinch-off.

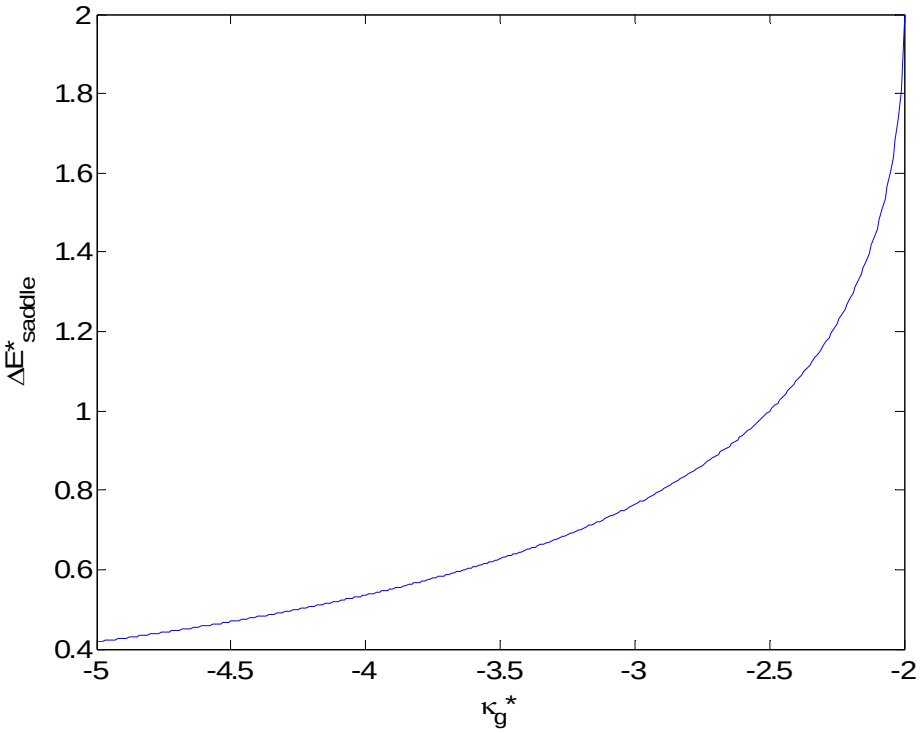

Figure 23 – Energy of saddle point in homogeneous membrane

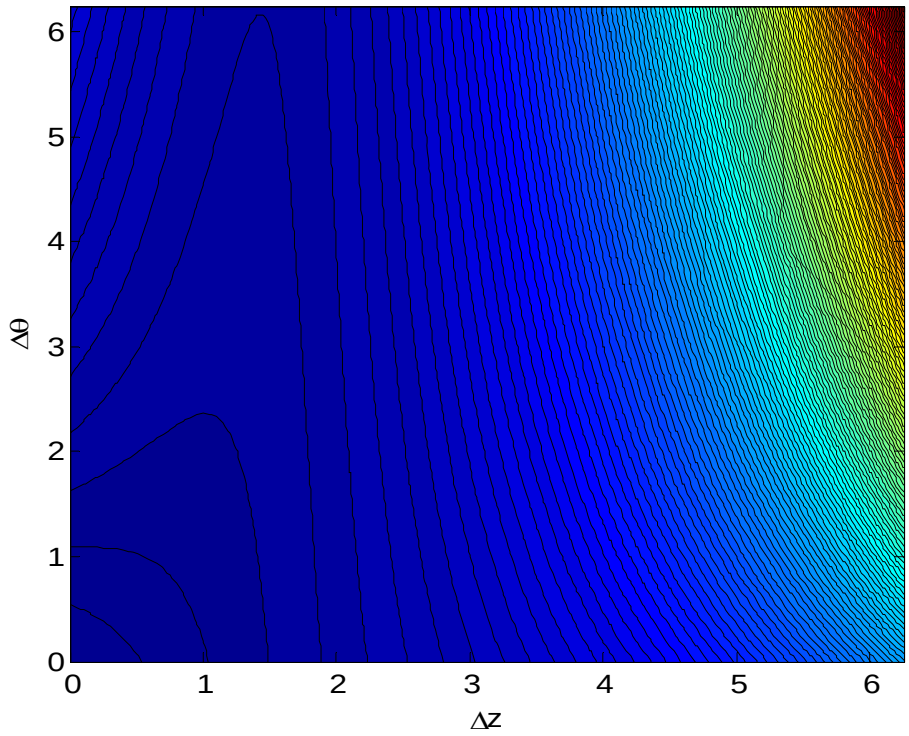

Figure 24 –Energetic landscape of homogeneous membrane for $\kappa_g^* = -1.9$. This figure demonstrates that the system has no physical equilibria for $\kappa_g^* > -2$.

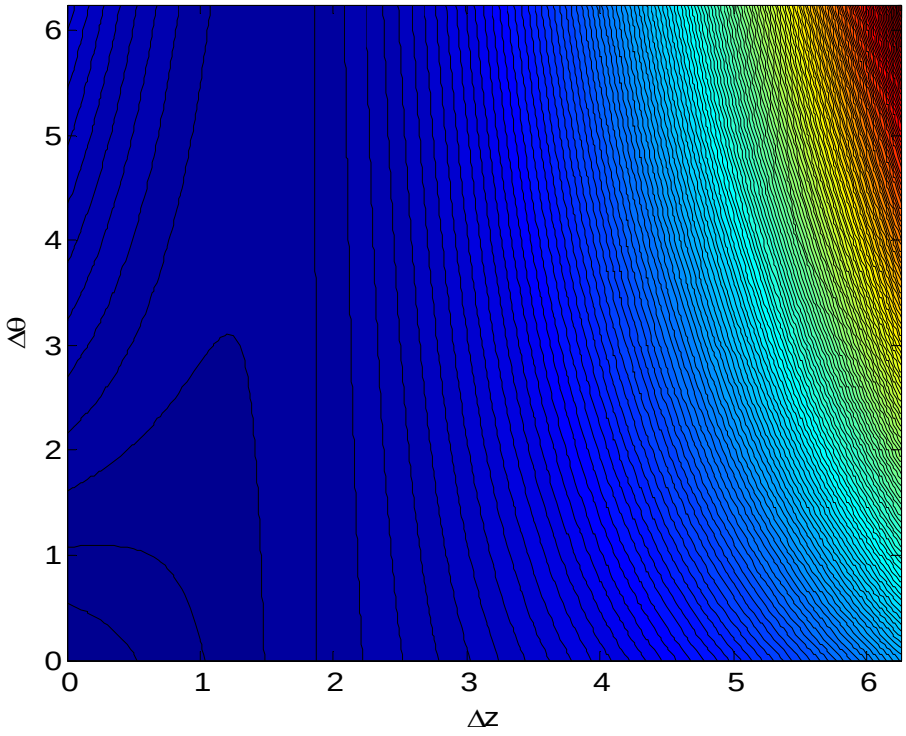

Figure 25 -- $\kappa_g^* = -2$. Onset of a stable pore at $\Delta\theta \rightarrow \infty$.

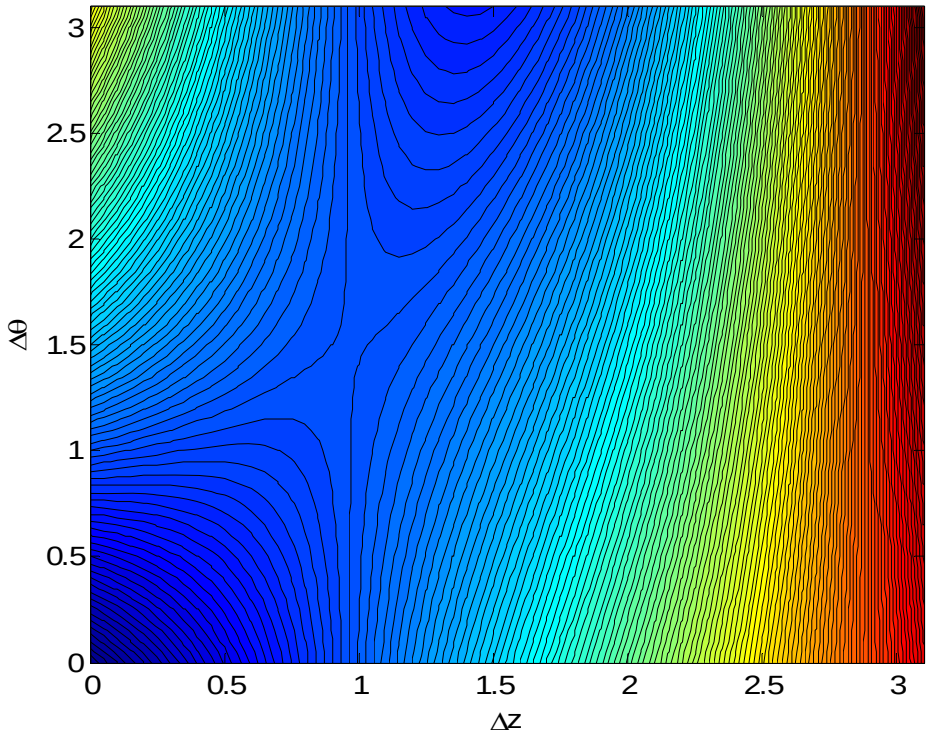

Figure 26 -- $\kappa_g^* = -2.5$. Note the axes have been changed to show more detail.

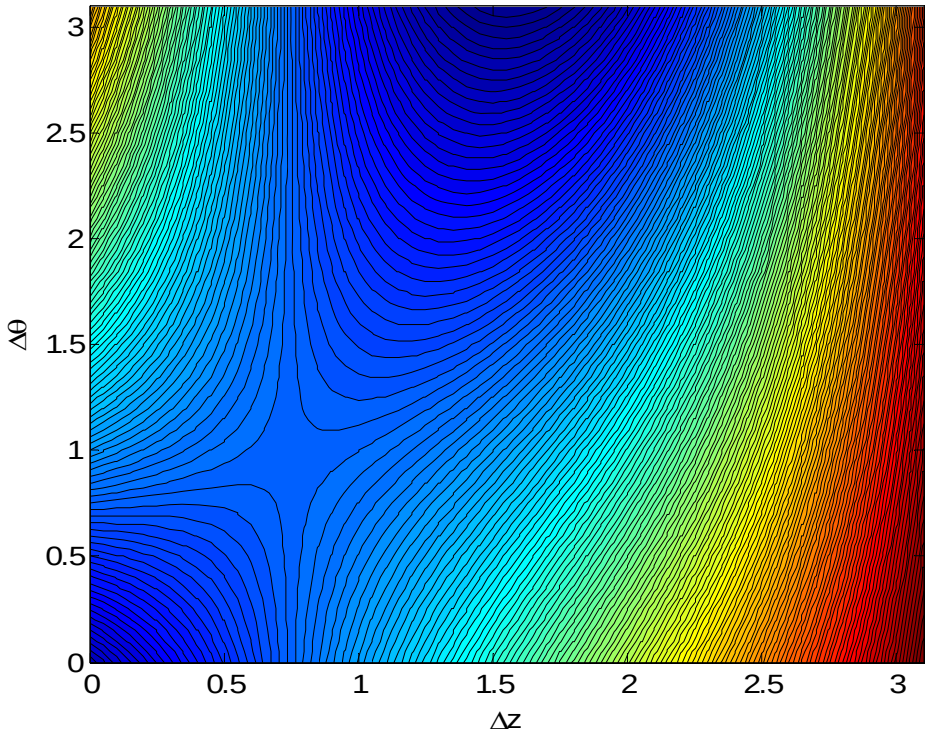

Figure 27 -- κ_g^* = -3.

5.4 PORE ENERGETICS WITH ADHESION

From the preceding, it is clear that for neck pinch-off to be driven by change in Gaussian energy, κ_g^* must be less than -2, with the activation energy for the pinch-off process given by Figure 3. However, if an adhesive surface, such as an engulfed particle, is in contact with the membrane, the surface promotes pore formation if the pore area is transferred to the surface. Pinch-off for membranes with $\kappa_g^* > -2$ is therefore possible. Adhesion introduces another energetic term to the Helfrich equation

$$\Delta E_{adhesion} = \int_{-\Delta z/2}^{\Delta z/2} \int_{-\Delta\theta/2}^{\Delta\theta/2} e_{adh} r(z) d\theta dz$$

where e_{adh} is the energy of adhesion per unit area. Substituting the caternary equation for $r(z)$,

$$\Delta E_{adhesion} = 2\Delta\theta e_{adh} R^2 \sinh(\Delta z / 2R)$$

We define dimensionless adhesion energy as $e^* = \frac{e_{adh} R}{\sigma_{edge}}$, and find that

$$\Delta E^*_{adhesion} = \Delta\theta e^* \sinh(\Delta z^* / 2)$$

Adding this term to the total energy, we have

$$\Delta E^* = \kappa_g^*(\Delta\theta)\tanh(\Delta z^*/2) + \left[(\Delta\theta)\cosh(\Delta z^*/2) + 2\sinh(\Delta z^*/2)\right] + \Delta\theta e^* \sinh(\Delta z^*/2)$$

5.5 EQUILIBRIUM PORE WITH ADHESION

Via the equilibrium criterion, we find that adhesion introduces an additional term to Equation 25:

$$\sinh^2(\Delta z_{eq}^*/2) + \kappa_g^* \sinh(\Delta z_{eq}^*/2) + 1 = -(e^*/2)\sinh(\Delta z_{eq}^*)$$

or

$$\sinh^2(\Delta z_{eq}^*/2) + \kappa_g^* \sinh(\Delta z_{eq}^*/2) + 1 = -e^* \sinh(\Delta z_{eq}^*/2)\sqrt{1 + \sinh^2(\Delta z_{eq}^*/2)}$$

Squaring both sides and rearranging, we have a quartic equation:

$$(1-e^{*2})\sinh^4(\Delta z_{eq}^*/2)+2\kappa_g^*\sinh^3(\Delta z_{eq}^*/2)+(2+\kappa_g^{*2}-e^{*2})\sinh^2(\Delta z_{eq}^*/2)+2\kappa_g^*\sinh(\Delta z_{eq}^*/2)+1=0$$

The solutions to such equations are cumbersome, but they do exist in closed form. In order to obtain $\Delta\theta_{eq}$, we apply the second equilibrium criterion. Differentiating and solving for $\Delta\theta_{eq}$,

$$\Delta\theta_{eq}=\frac{-2\cosh(\Delta z_{eq}^*/2)}{\kappa_g^*\sec h^2(\Delta z_{eq}^*/2)+\sinh(\Delta z_{eq}^*/2)+w^*\cosh(\Delta z_{eq}^*/2)}$$

We determine the critical parameter e_{crit}^* for emergence of a pore as a function of Gaussian modulus κ_g^*, $e_{crit}^*(\kappa_g^*)$, in the following manner. For each point κ_g^*, we determine the real and imaginary parts of the four roots of the associated quartic equation as a function of e^*. For instance, the imaginary parts of the roots of the equation with κ_g^* = -1.5 are shown in Figure 27, and the real parts in Figure 28. We determine e_{crit}^* as the first e^* with a strictly real, physical solution: $\mathrm{Im}(\Delta z^*)=0$, $\Delta z^*>0$, and $\Delta\theta>0$. This yields a plot of e_{crit}^*, shown in Figure 29.

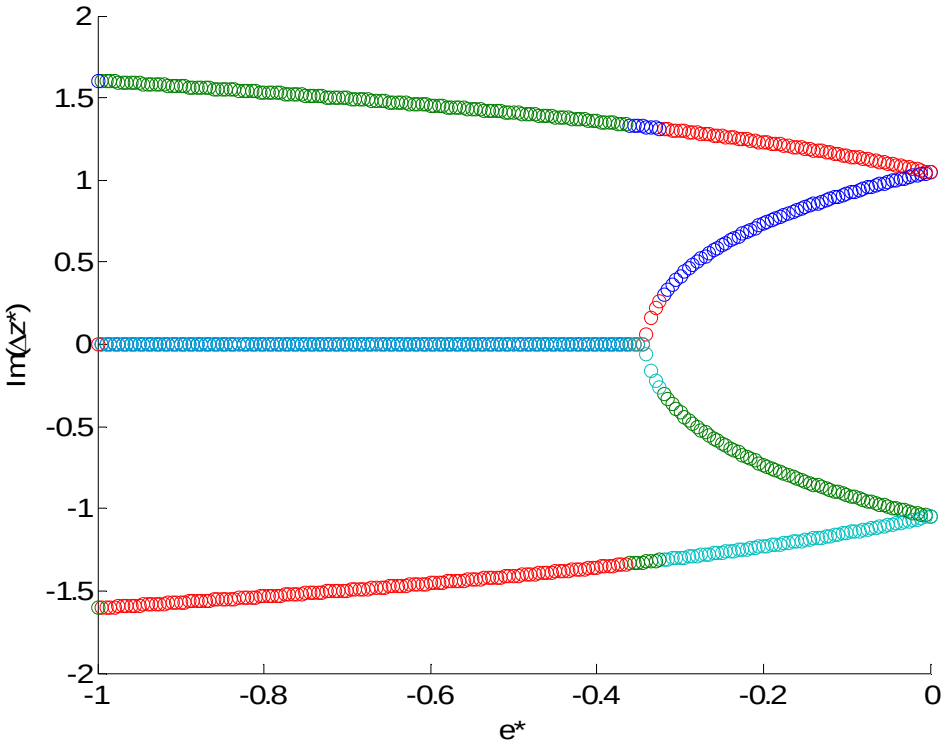

Figure 28 – Imaginary part of roots of quartic equation for $\kappa_g^* = -1.5$

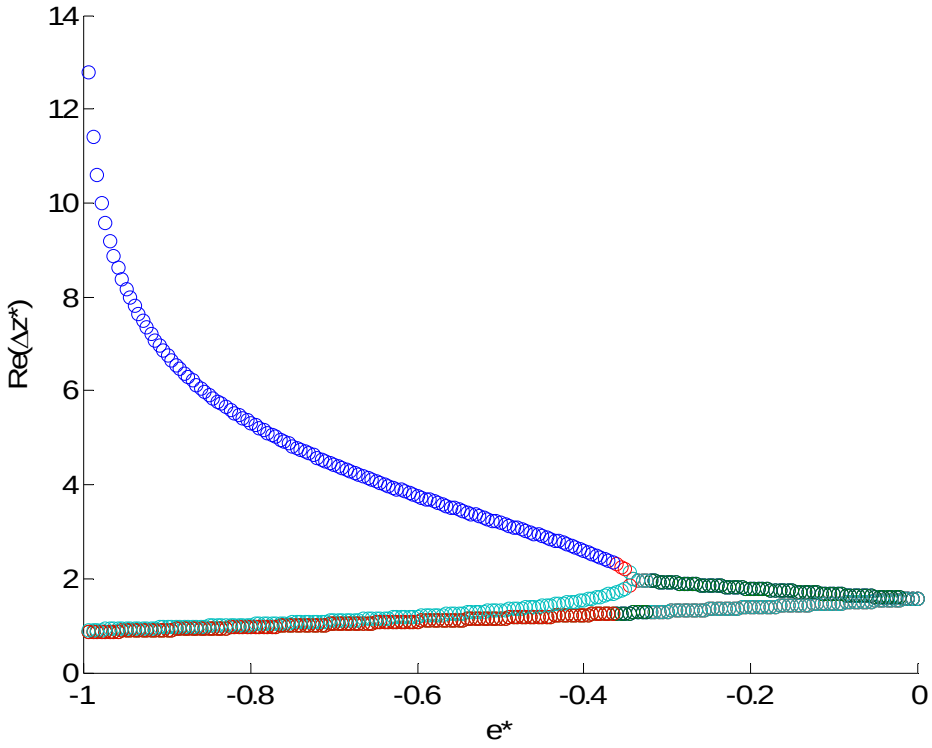

Figure 29 – Real part of roots of quartic equation for $\kappa_g^* = -1.5$

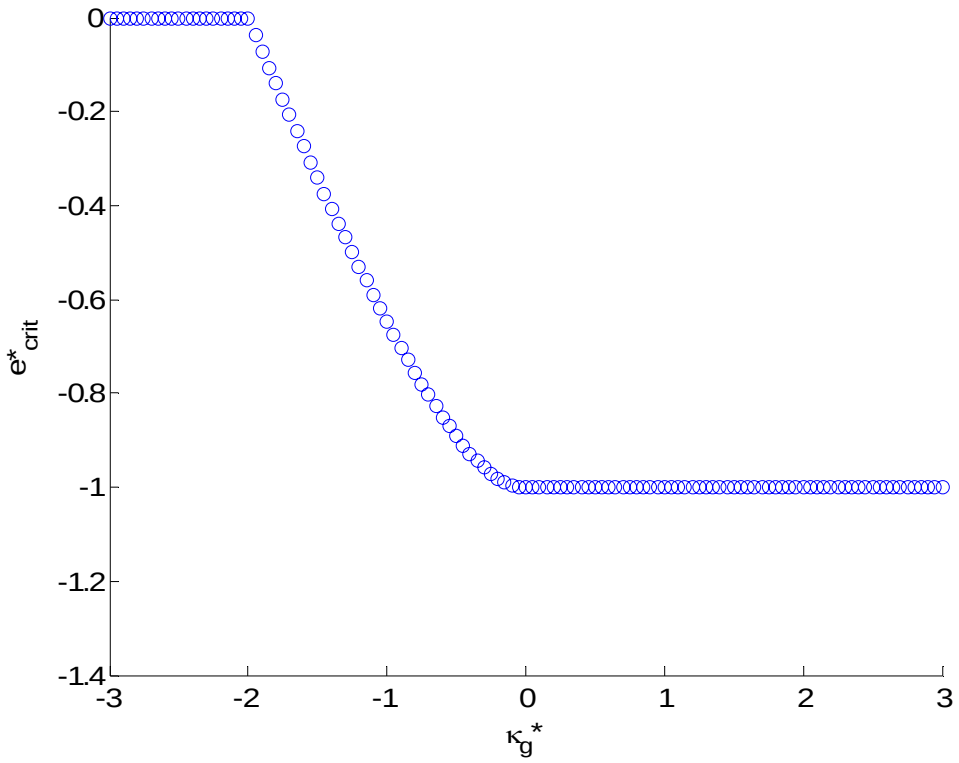

Figure 30 – Critical adhesion energy for emergence of a stable pore as a function of κ_g*.

As one would expect from the preceding subsection, for κ_g^* < -2, the critical value of the adhesion strength goes to zero; the pore can form spontaneously, driven by the gain in Gaussian free energy. For positive κ_g^*, a real solution emerges at $e^* = -1$ because the leading order term in the equation for energy is eliminated. For cubic equations, the existence of at least one real root follows from the intermediate value theorem. As before, we obtain saddle point solutions. We show examples in Figures 30 and 31. Energy is plotted in Figure 32 as a function of κ_g^* for various values of e^*.

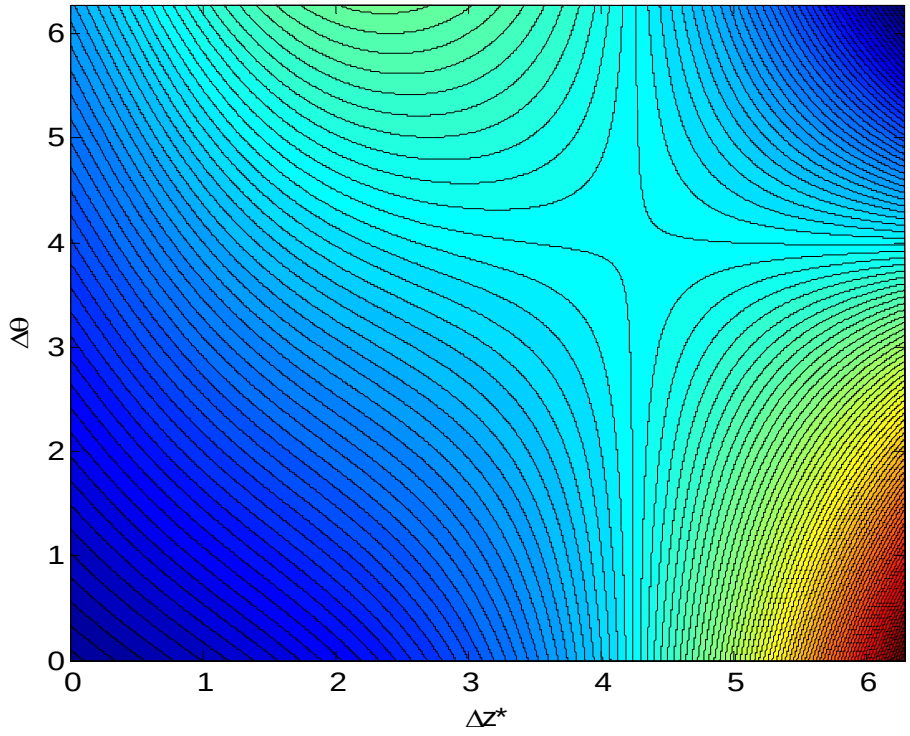

Figure 31 -- $\kappa_g^* = 2$, $e^* = -1.5$. This figure illustrates that a saddle point can exist for positive κ_g^*.

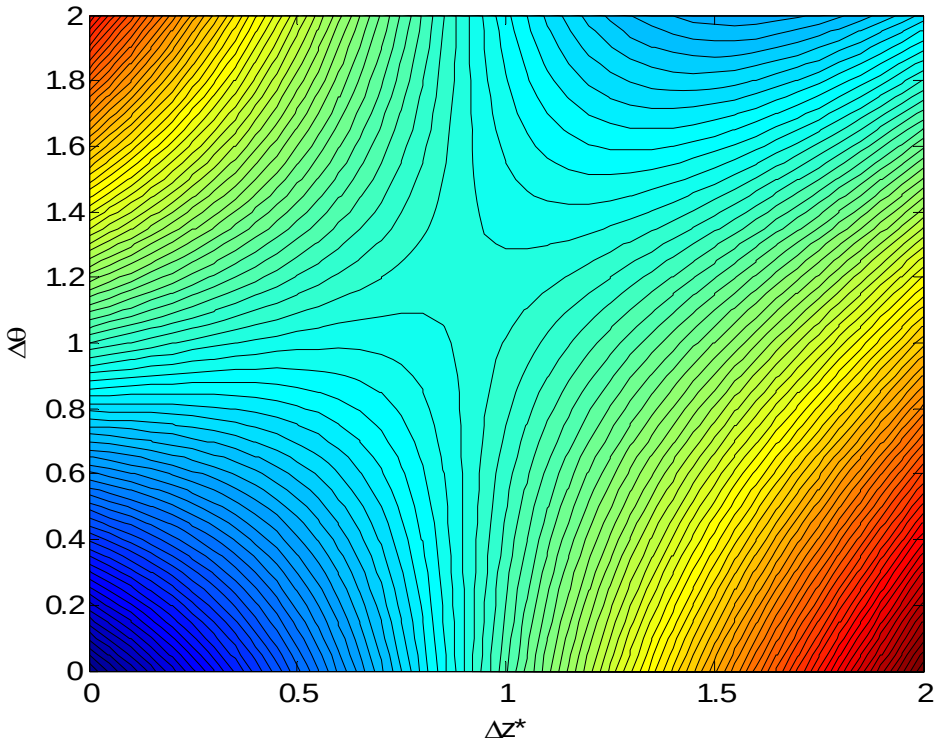

Figure 32 -- $\kappa_g^* = -1.5$, $e^* = -1$.

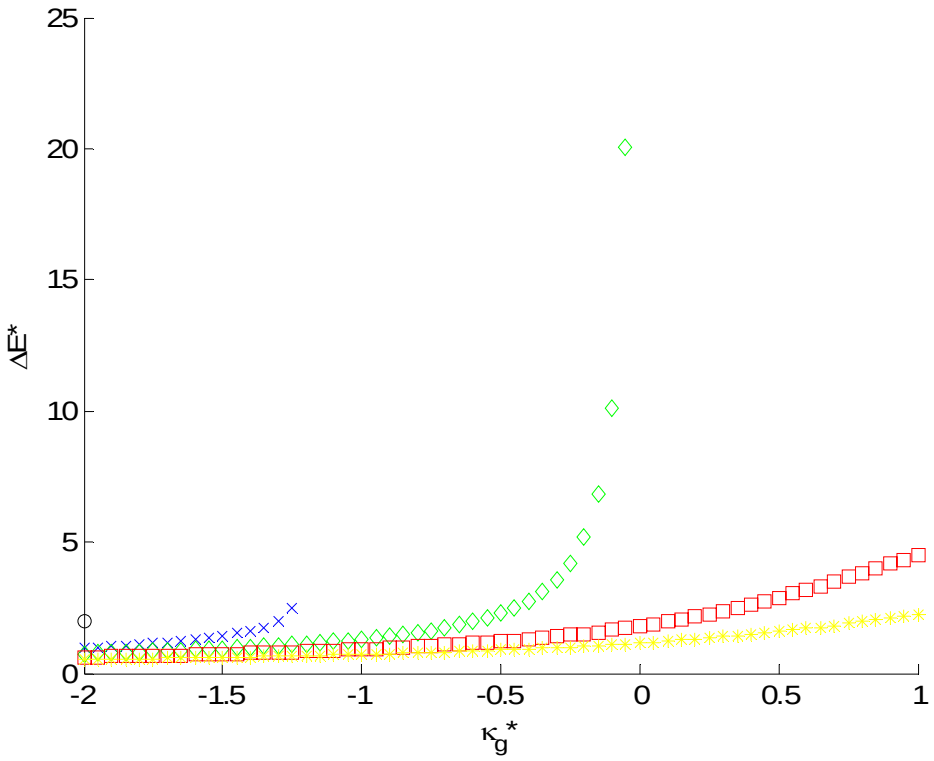

Figure 33 – Saddle point energy for a membrane in contact with an adhesive particle. For blue crosses, e* = -1.5; for green diamonds, e* = -1; for red squares, e* = -1.5; for yellow asterisks, e* = -2.

5.6 PORE ENERGETICS WITH INTERFACE

Finally, we examine the energetics of pore nucleation in the neck of a heterogeneous membrane. The interface between two lipid domains introduces a line tension:

$$E_{\text{int}} = \sigma_{\text{int}} \oint dl$$

The length is simply the circumference of the circle of revolution at the narrowest point of the neck, where the interface is located. Therefore, the change in energy given by the creation of a pore is

$$\Delta E = -\Delta\theta R\sigma_{\text{int}}$$

Nondimensionalizing,

$$\sigma_{\text{int}}^{*} = \frac{\sigma_{\text{int}}}{2\sigma_{edge}}$$

$$\Delta E_{\text{int}}^{*} = \frac{\Delta E_{\text{int}}}{2\sigma_{edge}R} = -\Delta\theta\sigma_{\text{int}}^{*}$$

We therefore have

$$\Delta E^{*} = \kappa_g^{*}(\Delta\theta)\tanh(\Delta z^{*}/2) + \left[(\Delta\theta)\cosh(\Delta z^{*}/2) + 2\sinh(\Delta z^{*}/2)\right] - \Delta\theta\sigma_{\text{int}}^{*}$$

for the free energy of a pore in a heterogeneous membrane.

5.7 EQUILIBRIUM PORE WITH INTERFACE

As before, we apply the equilibrium criterion, obtaining

$$\kappa_g^{*}\tanh(\Delta z_{eq}^{*}/2) + \cosh(\Delta z_{eq}^{*}/2) - \sigma_{\text{int}}^{*} = 0$$

$$\sinh^2(\Delta z_{eq}^{*}/2) + \kappa_g^{*}\sinh(\Delta z_{eq}^{*}/2) + 1 = \sigma_{\text{int}}^{*}\sqrt{1+\sinh^2(\Delta z_{eq}^{*}/2)}$$

Squaring both sides and rearranging, we again have a quartic equation:

$$\sinh^4(\Delta z_{eq}^{*}/2) + 2\kappa_g^{*}\sinh^3(\Delta z_{eq}^{*}/2) + (2+\kappa_g^{*2} - \sigma_{\text{int}}^{*2})\sinh^2(\Delta z_{eq}^{*}/2) + 2\kappa_g^{*}\sinh(\Delta z_{eq}^{*}/2) + (1-\sigma_{\text{int}}^{*2}) = 0$$

The solutions of this equation determine Δz_{eq}^{*}. To find $\Delta\theta_{eq}$, we apply the other equilibrium criterion. Since the reduction in interfacial energy does not depend on Δz^{*}, we find the same expression for $\Delta\theta_{eq}$ as in the homogeneous case:

$$\Delta\theta_{eq} = \frac{2\cosh(\Delta z_{eq}/2)}{-\kappa_g^* \sec h^2(\Delta z_{eq}^*/2) - \sinh(\Delta z_{eq}^*/2)}$$

As before, we calculate $\sigma^*_{\text{int},crit}$, shown in Figure 34. Of course, there are no saddle points for $\kappa_g^* > 0$, as the line energy is only a functon of $\Delta\theta$ and therefore can only drive angular growth of the pore.

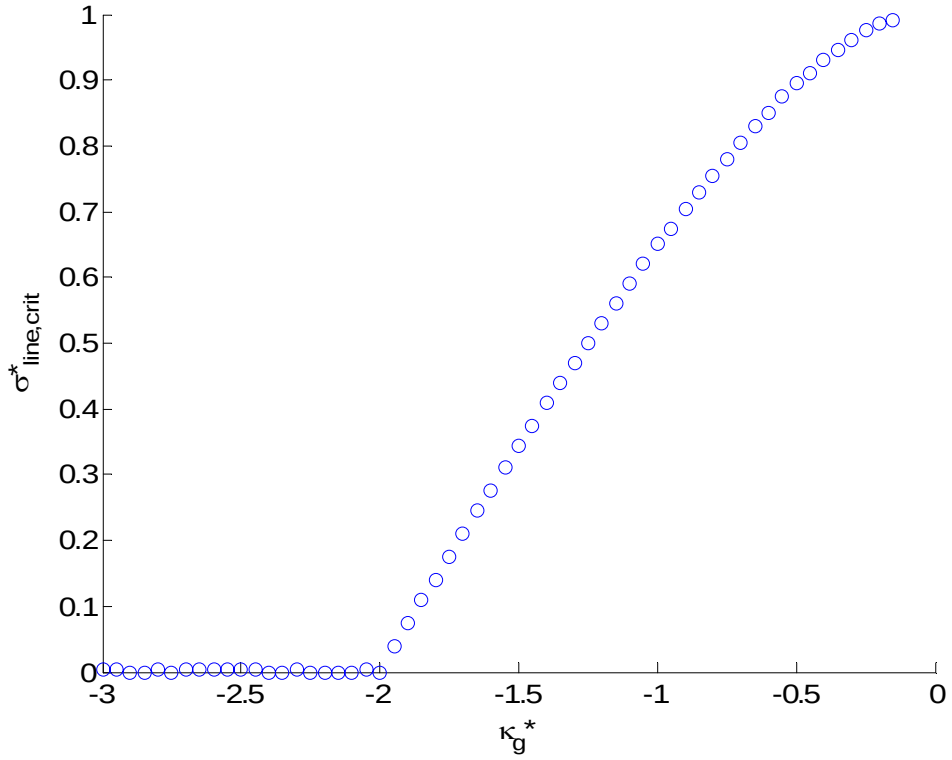

Figure 34 – Critical interfacial tension for formation of a stable pore as a function of κ_g*.

5.8 PREPARATION OF MEMBRANES WITH ADHESIVE PARTICLE

As noted above, we need only simulate two flat membranes connected by a catenoid neck, as the particle size is large relative to the membrane thickness h. We initially assemble two flat membranes connected by a cylindrical neck, with one membrane in contact with a solid wall. The number of lipids in the system is n.

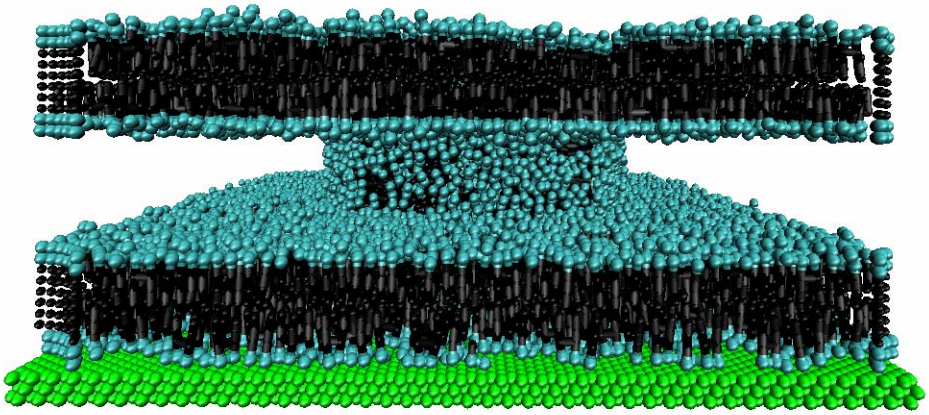

Figure 35 – Initial setup of membrane in contact with adhesive particle.

A cross section of the cylindrical neck is shown below:

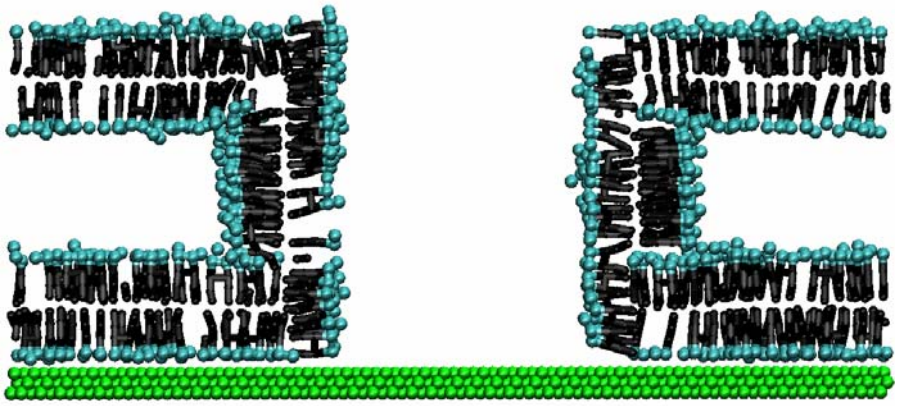

Figure 36 – Cross section of cylindrical neck.

In order to realistically simulate membrane dynamics, we introduce a rigid channel in the upper membrane. This channel allows solvent to pass from between the two membranes to the region above the upper membrane. Without this channel, the number of solvent particles in the region between the membranes would be constrained, artificially stabilizing the neck. In the membrane systems we are modeling, the region around the neck is open to the surrounding aqueous environment, allowing solvent to freely enter or leave the region. This channel is shown below:

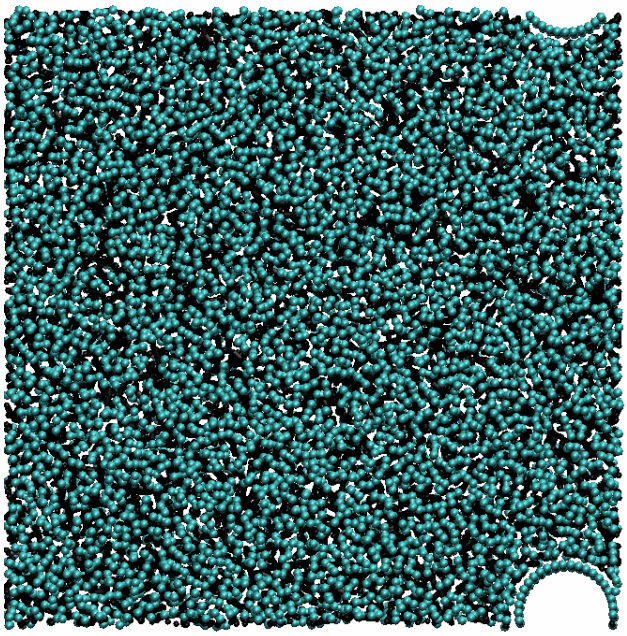

Figure 37 – Top-down view of membrane with rigid channel, allowing passage of solvent region to region above upper membrane.

With a_{PS} initially set to 25, we allow the system to relax over several thousand timesteps. The system assumes a catenoid neck with equilibrium radius $R(n)$:

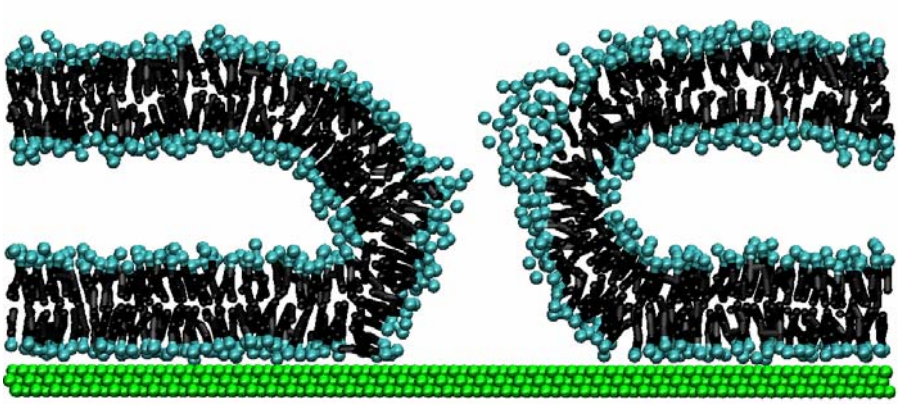

Figure 38 – Relaxed catenoid neck in cross section.

From this relaxed state, we vary $a_{PS} > 25$ and run the simulation for several thousand more timesteps. We determine whether the membrane ruptures for each a_{PS}, as well as the number of time steps to rupture.

5.9 PREPARATION OF MEMBRANE WITH INTERFACE

To simulate fission driven by an interfacial energy, we construct the system and allow it to relax as above. We then designate all lipid molecules with head groups below the catenoid neck midplane as type 2. We set the repulsion parameter $a_{H_1H_2} = a_{T_1T_2} > 25$, maintaining $a_{PS} = 25$. As before, we run the system for several thousand more time steps, determining the time to rupture.

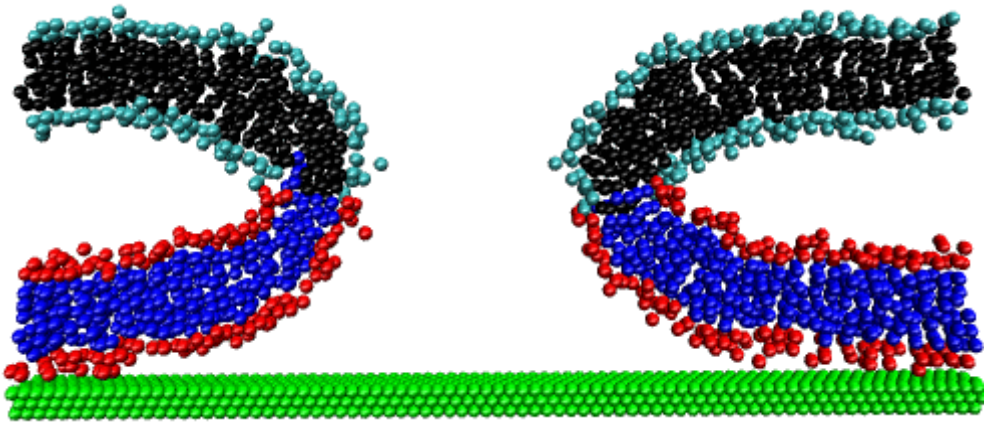

Figure 39 – Neck with interface in cross section.

5.10 SIMULATION RESULTS AND DISCUSSION

In membranes that rupture, small embryonic pores nucleate and close in the neck region until one achieves critical radius. Critically large pores quickly grow until they wrap entirely around the neck, separating the two upper and lower bilayers. The separated bilayers then close their resultant holes, eliminating the associated edge energy. This sequence is shown in Figures 40 through 42.

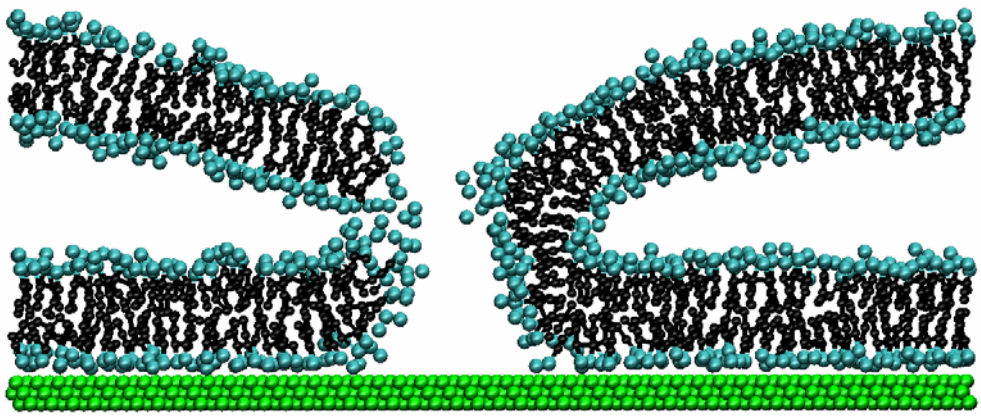

Figure 40 – A pore nucleates in the neck

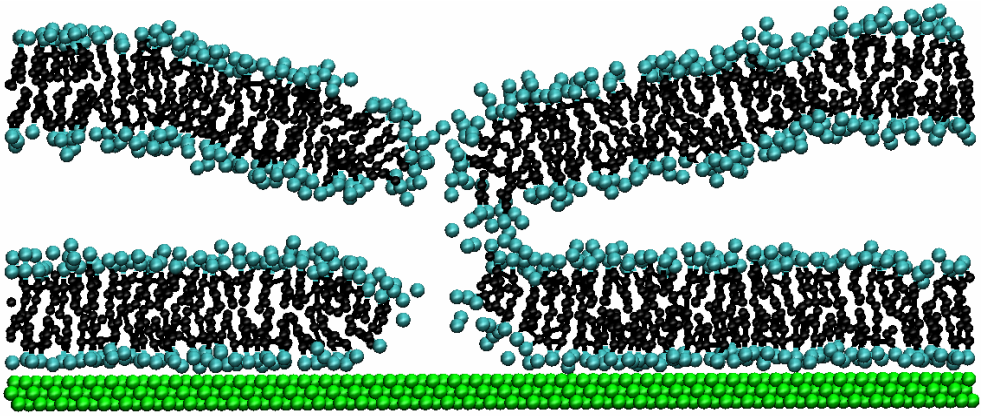

Figure 41 – The pore wraps around the neck, severing the two bilayers

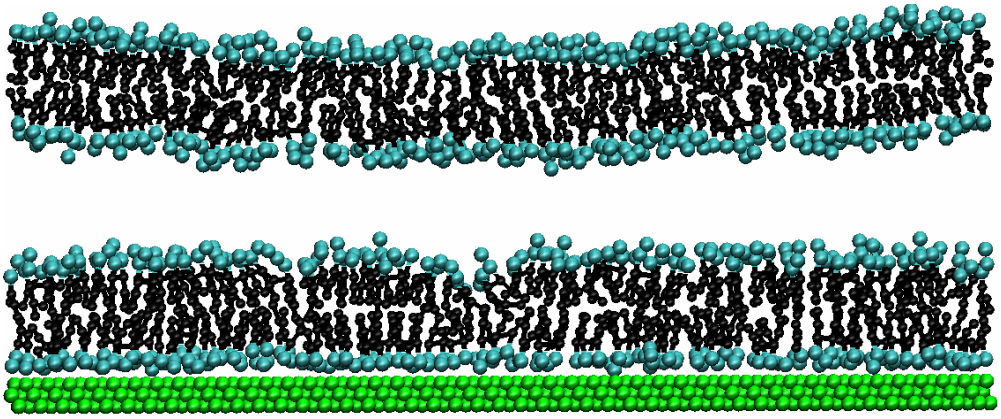

Figure 42 – The two separate bilayers completely close

5.11 CONCLUSIONS

A promising potential application of amphiphilic vesicles is in biomimetic phagocytosis, e.g. in remediation of nanoparticle environmental contaminants. Previous work in our group examined encapsulation of small particles, i.e. particles with radius on the order of the membrane thickness. That study delineated conditions for complete particle envelopment and vesiculation, but did not examine the mechanism of neck scission. In this work, we considered uptake of *large* particles. The scale of our study permitted investigation of pore nucleation and growth in the catenoid neck of the encapsulated particle. Since such necks are also formed in heterogeneous systems with large budded domains, we also considered membranes with an interface in the neck between two amphiphilic domains.

Via continuum elastic theory, we modeled pore energetics, determining the energy barrier to pinch-off and vesiculation. With dissipative particle dynamics, we studied the membrane/particle and heterogeneous systems numerically, observing neck behavior and recording the statistics of pinch-off events. Via the measurement of macroscopic elastic parameters from Section 3, we aim to connect the statistics of pinch-off to the elastic theory. Ultimately, we anticipate providing criteria for the design of vesicles for uptake of colloidal particles. Our preliminary results encourage us to continue our studies.

6.0 CONCLUSIONS

Bilayer vesicles and membranes will play an important role in microfluidics and soft, biomimetic nanotechnology. These supramolecular assemblies are composed of amphiphilic molcules, which self-assemble to shield their hydrophobic tail groups from solvent. In multicomponent systems, phase separated domains can form mushroom-like "buds" that protrude in the surrounding space, reducing interfacial energy. Via dissipative particle dynamics, a coarse-grained molecular simulation method, we investigated morphological and topological changes in multicomponent budded vesicles driven by imposed shear. We found that shear tends to flatten or detach the budded domain, depending on the position of the bud. We explain vesicle behavior on the basis of the interplay of shear, bending energy, and interfacial energy, providing criteria for the design of synthetic vesicles for controlled release. Budded synthetic vesicles could be tailored to controllably release their buds in targeted flow regions, e.g. in specific regions of the bloodstream.

In certain energetic conditions membranes can completely envelop adhesive colloidal particles. The neck of an encapsulated particle will assume a catenoid shape to eliminate bending energy. A previous study in our group examined uptake of small particles, outlining conditions for envelopment and pinch-off. However, the length scale of that study did not permit examination of the specific mechanism of neck scission. In this study we considered uptake of large particles, studying pore nucleation and growth in the encapsulated particle neck. Since

catenoid necks are also found in hetereogeneous systems, we also considered membranes with an interface in the neck between two lipid domains. We modeled pore energetics with continuum elastic theory, pinpointing the conditions for vesiculation and measuring the energy barrier of the pinch-off process. With dissipative particle dynamics, we simulated these systems numerically, measuring the statistics of pinch-off events. Ultimately, we aim to connect the elastic theory with the results of our numerical simulations. Preliminary simulation results, detailed in Section 5.10, encourage continued study.

REFERENCES

[1]P. Sens and M. S. Turner, Biophys. J. **86**, 2049 (2004).

[2]S. L. Veatch and S. L. Keller, Biophys. J. **85,** 3074 (2003).

[3]T. Baumgart, S. T. Hess, and W. W. Webb. Nature (London) **425**, 821 (2003).

[4]F. Julicher and R. Lipowsky, Phys. Rev. E **53**, 2670 (1996).

[5]D. P. Siegel, Biophys. J. **65**, 2124 (1993).

[6]M. Deserno and W. M. Gelbart, J. Phys. Chem. B **106**, 5543 (2002).

[7]M. Laradji and P. B. S. Kumar, J. Chem Phys. **123**, 224902 (2005).

[8]S. Yamamoto and S. Hyodo, J. Chem. Phys. **118**, 7937 (2003).

[9]Z. J. Wang and D. Frenkel, J. Chem. Phys. **123**, 154701 (2005).

[10]P. J. Hoogerbrugge and J. M. V. A. Koelman, Europhys. Lett. **19**, 155 (1993).

[11]R. D. Groot and P. B. Warren, J. Chem. Phys. **107**, 4423 (1997).

[12]P. Español and P. B. Warren, Europhys. Lett. **30**, 191 (1995).

[13]S. J. Plimpton, J. Comp. Phys. **117**, 1 (1995).

[14]R. Goetz and R. Lipowsky, J. Chem. Phys. **108**, 7397 (1998).

[15]R. Goetz, G. Gompper, and R. Lipowsky, Phys. Rev. A **44**, 1182 (1991).

[16]H. Strey and M. Peterson, Biophys. J. **69**, 478 (1995).

[17]W. Helfrich, in *Physics of Defects*, Les Houches Session XXXV, edited by R. Balian *et al*. (North Holland, Amsterdam, 1981).

[18]G. B. Jeffrey, Proc. R. Soc. London, Ser. A **102**, 161 (1922).

[19]B. J. Trevelyan and S. G. Mason, J. Colloid Sci. **6**, 354 (1951).

[20]E. J. Ding and C. K. Aidun, J. Fluid Mech. **423**, 317 (2000).

[21]D. W. Qi and L. S. Luo, Phys. Fluids **14**, 4440 (2002).

[23]H. A. Stone, Annu. Rev. Fluid Mech. **26**, 65 (1994).

[24]K. A. Smith, A. C. Balazs, D. M. Jasnow, in preparation.

[25]Y. Kozlovsky and M. M. Kozlov, Biophys. J. **85**, 85 (2003).